The Astronomical Journal, 162:33 (22pp), 2021 July https://doi.org/10.3847/1538-3881/abfd36

The Breakthrough Listen Search For Intelligent Life Near the Galactic Center. I.

Vishal Gajjar[1], Karen I. Perez[2], Andrew P. V. Siemion[1,3,4,5], Griffin Foster[1], Bryan Brzycki[1], Shami Chatterjee[6], Yuhong Chen[1], James M. Cordes[6], Steve Croft[1,4], Daniel Czech[1], David DeBoer[1], Julia DeMarines[1], Jamie Drew[7], Michael Gowanlock[8], Howard Isaacson[1,9], Brian C. Lacki[1], Matt Lebofsky[1], David H. E. MacMahon[1], Ian S. Morrison[10], Cherry Ng[1], Imke de Pater[1], Danny C. Price[1,10], Sofia Z. Sheikh[11], Akshay Suresh[6], Claire Webb[12], and S. Pete Worden[7]

[1] Department of Astronomy, University of California Berkeley, Berkeley, CA 94720, USA; vishalg@berkeley.edu
[2] Department of Astronomy, Columbia University, 550 West 120th Street, New York, NY 10027, USA
[3] Department of Astrophysics/IMAPP, Radboud University, Nijmegen, Netherlands
[4] SETI Institute, Mountain View, CA 94043, USA
[5] University of Malta, Institute of Space Sciences and Astronomy, Msida, MSD2080, Malta
[6] Cornell Center for Astrophysics and Planetary Science and Department of Astronomy, Cornell University, Ithaca, NY 14853, USA
[7] The Breakthrough Initiatives, NASA Research Park, Boulevard 18, Moffett Field, CA 94035, USA
[8] School of Informatics, Computing, and Cyber Systems, Northern Arizona University, Flagstaff, AZ 86011, USA
[9] University of Southern Queensland, Toowoomba, QLD 4350, Australia
[10] International Centre for Radio Astronomy Research, Curtin Institute of Radio Astronomy, Curtin University, Perth, WA 6845, Australia
[11] Department of Astronomy and Astrophysics, Pennsylvania State University, University Park, PA 16802, USA
[12] Massachusetts Institute of Technology, Cambridge, MA 02139, USA
Received 2020 October 7; revised 2021 April 16; accepted 2021 April 28; published 2021 June 29

Abstract

A line of sight toward the Galactic Center (GC) offers the largest number of potentially habitable systems of any direction in the sky. The Breakthrough Listen program is undertaking the most sensitive and deepest targeted SETI surveys toward the GC. Here, we outline our observing strategies with Robert C. Byrd Green Bank Telescope (GBT) and Parkes telescope to conduct 600 hr of deep observations across 0.7–93 GHz. We report preliminary results from our survey for extraterrestrial intelligence (ETI) beacons across 1–8 GHz with 7.0 and 11.2 hr of observations with Parkes and GBT, respectively. With our narrowband drifting signal search, we were able to place meaningful constraints on ETI transmitters across 1–4 GHz and 3.9–8 GHz with EIRP limits of $\geqslant 4 \times 10^{18}$ W among 60 million stars and $\geqslant 5 \times 10^{17}$ W among half a million stars, respectively. For the first time, we were able to constrain the existence of artificially dispersed transient signals across 3.9–8 GHz with EIRP $\geqslant 1 \times 10^{14}$ W/Hz with a repetition period $\leqslant 4.3$ hr. We also searched our 11.2 hr of deep observations of the GC and its surrounding region for Fast Radio Burst–like magnetars with the DM up to 5000 pc cm^{-3} with maximum pulse widths up to 90 ms at 6 GHz. We detected several hundred transient bursts from SGR J1745−2900, but did not detect any new transient bursts with the peak luminosity limit across our observed band of $\geqslant 10^{31}$ erg s^{-1} and burst rate of $\geqslant 0.23$ burst hr^{-1}. These limits are comparable to bright transient emission seen from other Galactic radio-loud magnetars, constraining their presence at the GC.

Unified Astronomy Thesaurus concepts: Technosignatures (2128); Galactic center (565); Magnetars (992); Neutron stars (1108); Radio transient sources (2008); Search for extraterrestrial intelligence (2127)

1. Introduction

The existence of intelligent life in the universe is one of the most profound and fundamental questions posed to science. Recent discoveries of habitable exoplanets and their prevalence (Howell et al. 2014; Dressing & Charbonneau 2015; Bryson et al. 2021) suggest that our Galaxy is likely to harbor life-bearing planets and perhaps technologically advanced civilizations. Advances in new instruments such as the James Webb Space Telescope will likely provide some pathway to "sniff" atmospheres of several dozen exoplanets to seek indirect evidence of life by detecting biosignatures. However, in many instances, such biosignatures are also expected to arise due to abiotic processes (see Wordsworth & Pierrehumbert 2014) and may not provide substantial and direct evidence of life. Moreover, these surveys will be limited to only a few hundred light years, will require long observations, and are unlikely to answer the question of whether any life discovered is intelligent. Surveys are underway to seek evidence of "technosignatures" (Tarter 2003) that can also provide indirect evidence of extraterrestrial intelligence (ETI). The Breakthrough Listen Initiative (BLI) is a US $100M 10 yr effort to conduct the most sensitive, comprehensive, and intensive search for technosignatures on other worlds across a large fraction of the electromagnetic spectrum (Isaacson et al. 2017; Worden et al. 2017; Gajjar et al. 2019).

Low-frequency electromagnetic waves, such as coherent radio waves, are prime candidates for such beacons because they are energetically cheap to produce and can convey information at maximum speeds across vast interstellar distances. Technosignature searches at radio frequencies take place in a large, multidimensional parameter space. Two of the most challenging parameters of any technosignature search include (a) the location of such putative ETI transmitters and (b) the transmission frequency of such signals. Along with these, unknown signal characteristics such as strength, intermittency, polarization, modulation types, and other unknown characteristics also play a significant role in measuring completeness of any search for extraterrestrial intelligence (SETI) survey (Tarter 2003; Wright et al. 2018). The Breakthrough Listen (BL) program mitigates some of these challenges by extending the search to a wide variety of targets across the entire electromagnetic spectrum

accessible from existing ground-based observing facilities. The BL program currently has dedicated time on three telescopes: the Robert C. Byrd Green Bank Telescope (GBT; MacMahon et al. 2018) and the *Parkes Observatory* (Parkes; Price et al. 2018) in the radio, and the *Automated Planet Finder* (APF; Lipman et al. 2019) in the optical. Additionally, commensal observations will soon begin at the *MeerKAT* radio telescope in South Africa. Gajjar et al. (2019) provides the current status of the above programs, as well as other observing facilities working alongside BL. The primary targets of the BL program include one million nearby stars, one hundred nearby galaxies, and deep observations of the Galactic Center (GC) and the Galactic plane (Isaacson et al. 2017). Enriquez et al. (2017) conducted one of the most sensitive surveys toward 692 nearby stars at 1.4 GHz as part of the BL program. More recently, Price et al. (2020) expanded this search to 1327 stars and extended the survey to 3.7 GHz. Further extending these surveys to more BL targets, in this paper, we outline details of our comprehensive survey of the GC with the BL program, along with early results.

1.1. Beacon Types and Survey Summary

There are two different ways of detecting evidence of ETI through radio technosignatures: detecting deliberate beacons, or eavesdropping on the leakage radiation that could be a byproduct of extraterrestrial technologies. However, it is much harder to speculate on the type of leakage radiation, and such putative leakage signals are also likely to be weaker. In this paper, we will focus on strong beacons deliberately transmitted by ETI. In the past, very few hours of observation on the GC have actually been performed to search for these ETI beacons. A narrowband Doppler-drifting beacon signal (Backus & Project Phoenix Team 2004; Harp et al. 2012) is a prime candidate for deliberately transmitted technosignatures. Shostak & Tarter (1985) carried out one of the few dedicated surveys of the GC for such narrowband signals in a 4 hr search with the Westerbork Synthesis Radio Telescope (WSRT) at a sensitivity threshold of $\sim 10^{18}$ W, reporting a nondetection.

Cole & Ekers (1979) suggest that, in addition to searching for signals concentrated in frequency space, searches for impulsive wideband signals should also be conducted. Powerful wideband radar systems are commonly used on Earth; they follow a dispersion relation similar to a pulse dispersed by the interstellar medium (ISM). An advanced society may know about pulsars and the techniques required to detect them. They could generate a pulsar-like broadband radar signal readily detected by another technologically capable society. Further, they could induce an artificial dispersion measure into the pulse to differentiate their transmitted signal from a pulsar. Such a signal serves as a second type of beacon readily identifiable as originating from nonastrophysical processes. Cole & Ekers (1979) further speculated that such broadband beacons will consist of extremely narrow ($\leqslant 4\,\mu$s) in time pulses (nonphysical) and conducted searches for naturally dispersed pulses toward many targets including the GC. However, the Crab pulsar is known to produce μs structures at higher frequencies (Hankins & Eilek 2007). Thus, negative or artificial dispersion might be the only indicator of artificiality for such broadband signals.

No other SETI survey with moderate sensitivity has been performed for the GC region. Given the potential for discovery in the GC region, our outlined survey will contiguously span the large fraction of visible radio window from ground-based facilities, i.e., from 1 to 93 GHz. This constitutes the largest fractional bandwidth search for radio signals toward any source to date for SETI. In Section 2, we highlight that the GC is one of the most interesting locations to conduct a survey for technosignatures, with Section 2.4 outlining the ancillary science benefits. In Section 3, we outline our survey strategy for the Parkes telescope (Section 3.1) and GBT (Section 3.2), which will conduct observations across 0.7–3.8 GHz utilizing 352 hr and 3.9–93.0 GHz utilizing 280 hr, respectively. In Section 4, we outline observations that have already been carried out across 1–8 GHz from both these facilities. In Section 5, we detail our search for two beacon types. Section 5.1 highlights our search for the abovementioned narrowband Doppler-drifting signals, while Section 5.2 outlines our searches for four different types of broadband dispersed signals (originating from natural and nonastrophysical processes). Section 6 discusses the implications of our findings, and Section 7 lists our final conclusions.

2. Galactic Center

2.1. Highest Number of Line-of-sight Targets

The GC has the largest concentration and highest number density of stars within the Galaxy. The line of sight toward the GC offers the largest integrated Galactic star count of any direction in the sky. However, the emergence of intelligence near the GC depends on the probability of habitable planets along with their survival and stability due to nearby frequent supernovae (SNae) and other cataclysmic events such as stellar flybys and flares from magnetars near the GC. Lineweaver et al. (2004) also indicated that the inner region might be a less hospitable environment for habitability. In Jiménez-Torres et al. (2013), it is found that, within $R = 0.8$ kpc of the GC, stellar flybys are likely to disrupt Oort clouds, which would consequently result in the damage of planetary disks and systems. However, such flybys might deplete the Oort clouds on a fairly short timescale, thus making the planetary systems *more* habitable at longer times. Gowanlock et al. (2011) modeled the habitability of the Galaxy to host complex land-based life. Morrison & Gowanlock (2015) assessed the propensity of the Milky Way to host intelligent life by including an additional timescale to the prior work of Gowanlock et al. (2011) that accounts for the transition from complex to intelligent life, which required 0.6 Gyr on Earth. Both these models suggest the inner Galaxy as the most likely place for the emergence of habitable worlds and intelligent life. However, Gowanlock et al. (2011) elected to model the Galactic disk only at $R \geqslant 2.5$ kpc, as the complicated formation history of the galactic bulge at $R < 2.5$ makes it difficult to model habitability in the region. To understand the propensity of intelligent life in the very inner region of the Milky Way for our BL survey, we update their model to account for the entire disk and include the $R < 2.5$ kpc region. As is clearly evident from Figure 1, the fraction of stars with a habitable planet is greatest in the inner disk of the Galaxy. This is because there is much earlier planet formation in the region than at the Solar neighborhood or the outskirts, due to the inside-out formation history of the Galaxy. Despite the high SNae rate in the inner Galaxy, there are more opportunities for land-based, subsurface, or oceanic complex life to emerge on planets in the region. The propensity for the emergence of intelligent life as introduced by Morrison & Gowanlock (2015) closely follows

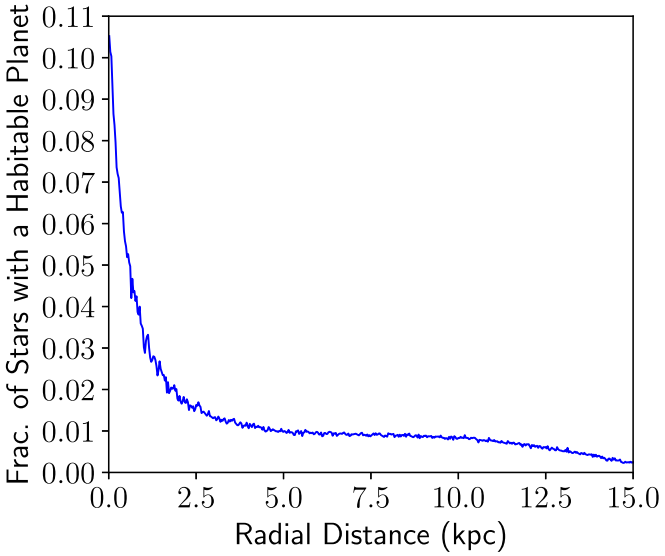

Figure 1. The fraction of stars with a habitable planet as a function of galactocentric radius, R, using the most conservative model in Gowanlock et al. (2011). The inner Galaxy hosts the greatest fraction of stars with a habitable planet.

the density of habitable worlds and thus also suggests the inner region of the Galaxy as the most promising region. In summary, with findings from Gowanlock et al. (2011) and Morrison & Gowanlock (2015), as well as our extension to the inner disk ($R < 2.5$ kpc), if the emergence of life is commonplace within the galaxy, it follows that the inner Galaxy, especially regions around the GC, would provide an ideal location to search for technosignatures in our Galaxy.

2.2. Spacefaring Societies

The higher density of stars and habitable planets at the GC will also be beneficial for the growth of more advanced societies. Close proximity among the likely inhabited worlds may accelerate development of interstellar communication and travel, which can give rise to advanced spacefaring societies. Newman & Sagan (1981) first discussed in detail diffusion of such advanced societies across the Milky Way. More recently, Carroll-Nellenback et al. (2019) modeled the expansion of spacefaring societies and suggested that the high density of stars provides settlement fronts to move much more quickly. Thus, if civilizations engage in settlements, planets in the inner region of the Galaxy are likely to be settled by advanced societies much earlier than other parts of the Milky Way. Similar arguments are used by Di Stefano & Ray (2016) to suggest that globular clusters are likely places to harbor spacefaring societies, due to their close proximity to each other. Such advanced societies are likely to produce technosignatures that can be detected across large interstellar distances.

2.3. Schelling Point

In game theory, Schelling (1960) suggested an approach by which different members of a group can derive a mutually beneficial solution to a problem in the absence of direct communication. These arguments can be extended to propose a range of parameter spaces that ought to provide a maximal outcome in searches for technosignatures (Wright 2018). For example, suggestions of searching near the hydrogen-line frequency by Cocconi & Morrison (1959) and within the "cosmic water-hole" frequencies by Oliver & Billingham (1971) provide likely "Schelling points" for suitable frequencies to search for ETI beacons. In order to maximize the chances of detecting beacons across the entire sky, the optimal Schelling point for such a transmitter to exist would be the GC. The GC is a natural cynosure of the entire Milky Way, and also suggested by Project Cyclops as the only likely direction for sensitive technosignature searches (Oliver & Billingham 1971).[13]

Benford et al. (2010a) argued various motivations for an advanced society to transmit powerful beacons and highlights the importance of an energy budget. They argued that transmitting strong pulses as beacons with a certain duty cycle would be the most cost-effective way to build a beacon. Benford et al. (2010a) suggested that advanced societies residing in our line of sight toward the GC might choose to transmit such powerful beacons toward the GC in order to get the maximum number of targets in the beam. Such transmitters might also direct back outward away from the GC because it is likely that societies like ours will be looking at the GC, due to the abovementioned Schelling point argument. They hence suggested a survey strategy to look at the GC on a roughly daily cadence over an annual period. Benford et al. (2010b) calculated the energy budget of such a strong beacon. As the required power for such a transmitter is proportional to the square of the distance to the target (i.e., $P_{\rm transmitter} \propto D^2$), placing a transmitter at a location that can illuminate a large fraction of targets in the Milky Way with the least amount of energy would also favor the GC. Recently, Comisso & Asenjo (2021) suggested that it is possible to extract energy from the spinning black hole at the GC. An advanced ETI transmitter might be able to obtain enough energy this way to remain active for billions of years. Thus, we propose that by placing a powerful transmitter either at the GC or pointing toward and away from the GC are the most cost-effective ways, making it an ideal Schelling point for technosignature searches within the Milky Way.

2.4. Ancillary Science

The GC region is also an exciting observational target for a host of natural astrophysical phenomena, prominently including pulsars in close orbits around the central supermassive black hole, Sgr A* and other magnetars, or in new exotic systems such as a millisecond pulsar in a binary system with a black hole.

2.4.1. Pulsars

Pulsars orbiting near the Galactic Center (Cordes & Lazio 1997; Pfahl & Loeb 2004) could offer unprecedented insights into the surroundings of its supermassive black hole of mass $\sim 4 \times 10^6 M_\odot$ (Ghez et al. 2008; Genzel et al. 2010). In particular, the discovery of a pulsar on a $\sim$1 yr orbit around Sgr A* will lead to high precision vetting of the theory of General Relativity in the strong field regime (Liu et al. 2012). So far, the nearest pulsars discovered are 10–15′ away, or approximately 30 pc in projection (Johnston et al. 2006; Deneva et al. 2009), despite the expectation of a large population of close-in neutron stars. Our survey data are already being utilized for deep searches for regular and millisecond pulsars, which will likely provide some of the

[13] However, this is due to our current limitations in surveying all-sky across all frequencies with compelling sensitivities.

most stringent constraint on the presence of pulsar populations within the central 1 pc region (Suresh et al. 2021, in preparation).

2.4.2. SGR J1745−2900

The exciting discovery of a radio magnetar, SGR J1745−2900, at a projected distance of 0.1 pc from the GC (Eatough et al. 2013a) was originally detected as an X-ray flare by the Swift observatory (Degenaar et al. 2013; Kennea et al. 2013), and then shown to repeat with a spin period of 3.76 s by NuSTAR (Mori et al. 2013). Radio pulsations of this source were thereafter detected at frequencies ranging from 1.2 to 18.95 GHz (Spitler et al. 2014). The estimated dispersion measure (DM) for the source is 1778 ± 3 pc cm^{-3}, and the rotation measure (RM), -66960 ± 50 rad m^{-2}, is the highest RM value for any known Galactic source. Eatough et al. (2013b) suggested the RM is consistent with a large magnetic field pervading the plasma surrounding the supermassive black hole. Surprisingly, however, the observed scattered profiles were measured to have a scattering time of 1.3 s at 1 GHz, much less than predicted by the scattering models (Spitler et al. 2014). Bower et al. (2014) obtained the first very long baseline interferometry (VLBI) image of the GC magnetar, and measured an angular size of approximately $\theta = 130$ mas at 8.7 GHz, similar to that of Sgr A* itself. Since SGR J1745−2900 is so close to the GC region (only 2.″4 from the GC), even at our highest survey frequency of 93 GHz (10″ beam with the GBT), it will be well within our central beam. Thus, our survey will observe SGR J1745−2900 across 0.7–93.0 GHz. This will allow a detailed study of spectro-temporal properties of numerous bursts and evolution of the integrated profile.

2.4.3. Fast Transients

Fast Radio Bursts (FRBs) are highly dispersed, millisecond duration bursts of unknown origin. Even a decade since their discovery, they are one of the most exciting challenges for modern astrophysics. Due to the DM excess beyond the Milky Way contribution and excellent interferometric localization of around a half-a-dozen sources, they have been revealed to be extragalactic in origin. There are a number of theories that have been proposed to explain the origin of FRBs. Among them, highly magnetized neutron stars such as magnetars have been favored as one of the most likely origins. This is further supported by the recent detection of Galactic magnetar SGR 1935+2154 (The CHIME/FRB Collaboration et al. 2020; Bochenek et al. 2020). This luminous Galactic FRB-like magnetar (with radio luminosity $\approx 10^{38}$ erg s^{-1}) was only detected as single pulses (The CHIME/FRB Collaboration et al. 2020; Bochenek et al. 2020; Zhang et al. 2020), and prolonged observations looking for regular pulsation through harmonic searches were unsuccessful (Surnis et al. 2020a, 2020b). Finding more such Galactic radio-loud magnetars and studying their spectro-temporal properties would likely help us solve the origin mystery of FRBs.

Dexter & O'Leary (2014) suggested that the GC is likely to harbor a significant population of magnetars. Radio magnetars have been seen to show bright transient radio bursts (Camilo et al. 2006) with emission across a wide range of frequencies, as the GC magnetar (SGR J1745−2900) has been detected all the way up to 225 GHz (Torne et al. 2015). Spectra of the radio-emitting magnetars are remarkably flat (Camilo et al. 2007; Levin et al. 2010a; Torne et al. 2015), differing from normal pulsars that typically have steep flux spectra ($S_\nu \propto \nu^{-1.4}$). For example, Camilo et al. (2006) also reported bright transient radio pulses from XTE J1810−197 all the way up to 42 GHz. This means that magnetars can be considerably brighter than pulsars at higher frequencies. Recently, Gajjar et al. (2020) reported a detection of Swift J1819.0−0167 across 4–11 GHz, which has also been suggested as a magnetar candidate with a rotation period of around 1.3 s. Moreover, Gajjar et al. (2020) reported that Swift J1819.0−1607 was seen to emit only single bright pulses from 4–11 GHz, instead of regular weaker pulses. This suggests that bright radio pulses can be observed at higher frequencies from magnetars. *Does the GC region harbor a population of FRB-like Galactic magnetars?* With our survey, we will be able to search for such bright pulses all the way from 0.7 GHz to 93 GHz originating from any putative recently active magnetars from the GC region.

Other sources producing prominent transient emission include rotating radio transients (RRAT) and pulsars producing giant pulses (GPs). We will be sensitive to such sources at lower frequencies from our survey; however, the spectral indices of these sources are relatively steep, making their detection challenging across most of our observing bands.

3. Observation Strategy

Our strategy is to split these observations into two modes: shorter ON–OFF observations of the GC (0, 0)[14] and the surrounding region, and deep observations of just the GC (0, 0) region. The shorter observations will be conducted with three ON–OFF cadences with 5 minute and 10 minute pointings for GBT and Parkes, respectively. For Parkes, we doubled the length of individual scans, due to the significantly higher sky temperature ($T_{\rm sky}$) at lower frequencies toward the GC. Such ON–OFF pointing techniques have previously been used in BL observations of nearby stars by Enriquez et al. (2017) and Price et al. (2020). In order to keep optimum observing efficiency, for OFF pointings, we will use pointings that are at least two half-power beamwidth (HPBW) away from the same GC sampled region.

Interstellar scintillation induces intermittency in otherwise steady signals and will have timescales dependent on the degree of scattering (Cordes & Lazio 1991; Cordes et al. 1997). Consequently, the preferred observing strategy for the GC is to observe a target at multiple epochs. Thus, in order to discriminate such highly scintillating signals, we aim to conduct longer scans toward the GC (0, 0), which will be divided into multiple epochs spread over a few days. Such deep observations will also help us search for transient signals from ETIs and other astrophysical sources with lower duty cycles.

It should be noted that terrestrial interference makes identification of truly sky-localized narrowband signals a challenging task, especially for such deep observations where we are not planning to conduct similar-length OFF-pointing observations. At the GBT, all the receivers at frequencies higher than *X* band (>12 GHz) have multiple beams, which will allow a natural discrimination of sky-localized narrowband signals for our planned longer scans. For the Ultra Wideband Low (UWL) receiver at Parkes, along with the *C*-band and *X*-band receivers at the GBT, we aim to utilize the effects of the

[14] Because the beam size varies as a function of frequency, we refer to the central pointing on the GC for each observed band as GC (0, 0).

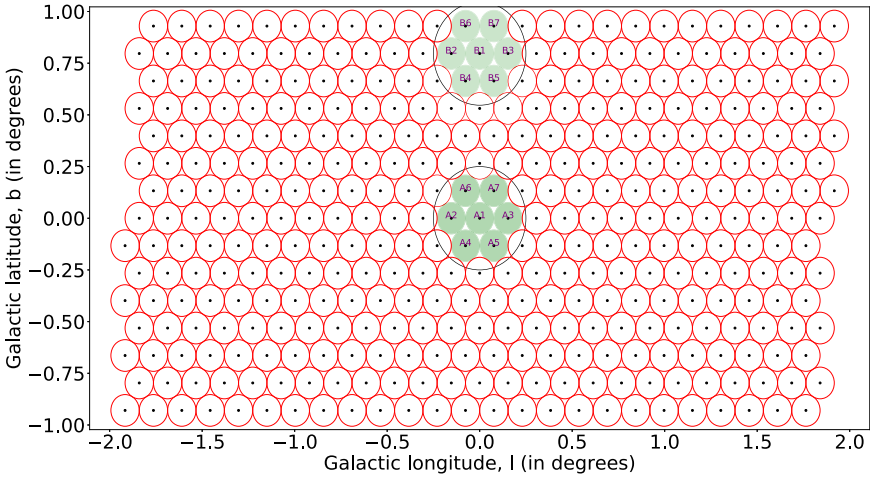

Figure 2. All 375 Parkes pointings planned to be surveyed with the BL GC survey. Each pointing, indicated with red solid circles, corresponds to the HPBW of the central frequency of the UWL receiver. All of the green pointings have already been observed and reported in this paper. The black circle indicates the HPBW of 30′, which corresponds to the lowest frequency of the UWL receiver. The pointings inside the central 30′ region are denoted A1–A7, while the corresponding OFF-source pointing are denoted B1–B7.

ISM on such narrowband signals to discriminate them from terrestrial interference using state-of-the-art machine-learning techniques. Such techniques are currently being explored by the BL team (Brzycki et al. 2020) and will be discussed in a future publication.

3.1. Parkes Telescope

We will use 352 on-source hours to observe the GC (0, 0) and bulge using Parkes. Parkes will perform the lower-frequency portion of the survey with the use of the newly installed UWL. This receiver covers 704 MHz to 4.032 GHz, with an average system temperature, $T_{\rm sys} = 22$ K˙ (Hobbs et al. 2020). Because we will only be using one receiver and the HPBW of Parkes is larger than that of the Green Bank Telescope (GBT), the observing strategy will be to observe with approximately half the time spent on the GC (168 h) and the remaining time surveying the bulge.

At 700 MHz, the HPBW is approximately 30′. This defines the Galactic Center for the Parkes observations. At a distance of 8.2 kpc (distance to the GC; Gravity Collaboration et al. 2019), this corresponds to a circular region with a radius of ∼35 pc. We plan to sample this region by using seven beams at a distance of 9.′2 from each other; this corresponds to the HPBW at the midpoint of the frequency band for the UWL (2.35 GHz). This is shown in Figure 2. We allocate approximately 24 h per pointing. Each pointing will be observed multiple times in 2–3 hr increments, at a cadence of every 1–2 weeks, to identify transient and highly scintillating signals. Our search parameters include a range of ± 4 Hz s^{-1}, which is large enough to account for changes in the Doppler shifts due to Earth's spin, taking orbital velocity effects to be negligible, toward the GC on different days of observations.

The Galactic bulge will be surveyed for 184 h. We define a region of 2° in Galactic latitude and 4° in Galactic longitude to cover the extent of the bulge. This corresponds to 375 pointings, including the abovementioned GC pointings. This will result in 30 minutes per pointing, with three ten-minute-long scans per pointing.

3.2. Green Bank Telescope

The GBT will be used for the high-frequency component of the survey starting from 4 GHz (*C* band) to 93 GHz (*W* band) (see Table 1) with a total observing time of around 280 h (excluding overhead). As mentioned earlier, a significant amount of observing time per receiver band will be dedicated for deep observations of the GC (0, 0). The remaining time will be used to observe the region around the GC. Many of the details in this section are taken from the GBT Proposer's Guide[15] and Observing Guide.[16]

We would like to uniformly sample the GC region with the complete observable GBT band. However, the GBT beam size varies by a factor of 30 and the receiver SEFDs cover a factor of 10 in sensitivity from *C* band to *W* band. Also, the instantaneous bandwidth varies between receiver. As such, a compromise in survey area, bandwidth, and sensitivity must be made. The observation pointings and integration times are summarized in Figure 4 and Table 2. A deep integration, similar to the Parkes observing plan will be performed with each receiver of the GC (0, 0). The GC bulge around GC (0, 0), depending on the beam size and number of sub-bands to cover the full receiver bandwidth, will also be sampled at 15 minute integration times (three five-minute scans). Further details of the receiver specific observing strategies are presented below.

C Band (3.9–8 GHz) The *C*-band feed is a dual-polarization, single-beam receiver with 3.9 GHz of instantaneous bandwidth. This feed has been used in previous BL observations of the standard target list (Isaacson et al. 2017), stars located in the restricted Earth transit zone (Sheikh et al. 2020), and FRB 121102 (Gajjar et al. 2018). A 4′ region around the GC can be fully sampled with 19 pointings, including a deep pointing of the GC (Figure 3). The BL digital backend (BLDB; MacMahon et al. 2018) will record baseband voltages across the entire 4 GHz of the receiver bandwidth. Combining the deep pointing of GC (0, 0) for 10 hr with the standard ON–OFF pointings of the 4′ bulge, we spent around 14 hr surveying the GC region. Detailed analysis of these observations is presented in Sections 4.1 and 5.

[15] https://science.nrao.edu/facilities/gbt/proposing/GBTpg.pdf
[16] https://science.nrao.edu/facilities/gbt/observing/GBTog.pdf

Table 1
Parkes Low-frequency and GBT High-frequency Receiver Bands Along with Other Necessary Details

Receiver	Obs. Freq. (GHz)	$N_{\rm beams}$	$N_{\rm bands}$	$\Delta\nu$/band (GHz)	Total $\Delta\nu$ (GHz)	Beam Size FWHM	SEFD (Jy)
UWL	0.704–4.032	1	1	4	4	9′2	40
C	3.9–8	1	1	4	4	2′5	10
X	8–11.6	1	1	2.4	2.4	1′4	15
Ku	12–15.4	2	1	3.5	3.5	54″	18
KFPA	18–27.5	2	2	8	9	32″	20
Ka	26–39.5	2	3	4	12	22.″6	25
Q	38.2–49.8	2	2	4	8	16″	60
W	67–93	2	4	6	24	10″	100

Note. Columns list range of covered frequencies, number of beams, number of sub-bands, instantaneous bandwidth per sub-band, total bandwidth, full width at half maximum (FWHM) beam size computed for the central frequency, and system equivalent flux density (SEFD), respectively. KFPA is a seven-beam receiver; however, we are only planning to use two of these beams, with 4 GHz of band per beam, for our survey.

Table 2
Observing Time and Number of Pointings for Parkes UWL and Each GBT Receiver Planned to Be Used in This GC Survey

Receiver	Sampled Region	Obs $\Delta\nu$ (GHz)	Deep pointings, $N_{\rm Int,deep}$	Obs Time per deep pointing, $\tau_{\rm obs,deep}$ (hours)	Bulge pointings, $N_{\rm Int,bulge}$	Obs Time all bulge pointings, $\tau_{\rm obs,bulge}$ (hours)	Total Obs (Hours)
UWL	$2^\circ \times 4^\circ$	4	7	24	368	184	352
C	$4' \times 4'$	4	1	10	18	4.5	14.5
X	$4' \times 4'$	2.4	1	10	36	9	19
Ku	$4' \times 4'$	3.5	1	10	126	31.5	41.5
KFPA	$2' \times 2'$	8	2	10	90	22.5	42.5
Ka	$2' \times 2'$	4	3	3	180	45	54
Q	$2' \times 2'$	4	2	3	180	45	51
W	$1' \times 1'$	6	4	2	144	36	44

Notes. The columns list the sampled region around the GC, available instantaneous bandwidth, number of deep pointings necessary to cover the full bandwidth at a given band and to fully sample GC (0, 0), total observation time per each deep pointing, total number of bulge pointings, total observing hours for the bulge, and total observing hours for the full survey at a given band, respectively. The total observing hours for each receiver are calculated as $N_{\rm Int,deep} \times \tau_{\rm obs,deep} + \tau_{\rm obs,bulge}$.

X Band (8.0–11.6 GHz) The *X*-band feed is a circularly polarized, single-beam receiver with 2.4 GHz of instantaneous bandwidth even though the total receiver bandwidth is 3.6 GHz. We aim to sample a 4′ region around the GC with 37 pointings, including a deep 10 h pointing of the GC (0, 0) (Figure 4(a)) with a total observing time of around 19 h.

Ku Band (12.0–15.4 GHz) The *Ku* band has two beams at a fixed separation (5′.5 in the cross-elevation direction), and each is circularly polarized. The instantaneous bandwidth is 3.5 GHz. Since the offset beam is likely to be outside the selected GC region for most of the GC pointings, it will be used to increase the sky coverage and to provide OFF sources for GC-region pointings. The BLDB is capable of recording 8 GHz of instantaneous bandwidth. This will allow us to capture full receiver coverage simultaneously from both beams, which will eliminate the need for ON-OFF cadence scans. A 4′ region around the GC will be fully sampled with 127 pointings, including a deep pointing of the GC (0, 0) (Figure 4(b)) with a total observing time of 41.5 h.

K-Band Focal Plane Array (18.0–27.5 GHz) The *K*-band receiver is a focal plane array (KFPA) of seven dual-polarization (circular) beams at fixed separations on the sky in a hexagonal pattern. The 2′ region around the GC can be fully sampled with 91 pointings as shown in Figure 4(c) considering an HPBW of 32″. There is a full seven-beam mode at 1.8 GHz instantaneous bandwidth per beam, and a dual-beam 8 GHz total instantaneous bandwidth experimental mode. Since the BL backend can capture 12 GHz of instantaneous bandwidth, we will use the single central beam with 8 GHz simultaneous bandwidth. For KFPA, we plan to use an ON–OFF observing strategy similar to that employed for the *C* band and *X* band. For the deep integration of the GC (0, 0) region, we plan to use the dual-beam mode of the KFPA with 4 GHz per beam. This doubles the number of independent pointings, to cover the entire bandwidth for the deep GC (0, 0) pointing. Such a dual-beam approach is especially necessary for transient signals, as dispersion delays at these frequencies are negligible, which renders them indistinguishable from radio-frequency interference (RFI). The 90 pointings of 15 min each from the GC bulge and two pointings (4 GHz per pointing) of 10 h each for GC (0, 0) gives a total observing time of 42.5 h.

Ka Band (26.0–39.5 GHz) The *Ka*-band receiver consists of two beams, each with a single polarization (linear) at a fixed separation (78″ in the cross-elevation direction). The beams are orthogonal in polarization. The band is split into three bands (26.0–31.0 GHz, 30.5–37.0 GHz, 36.0–39.5 GHz), only one of which can be used at a time, with an instantaneous bandwidth of 4 GHz. Thus, we will use both beams with 4 GHz per beam

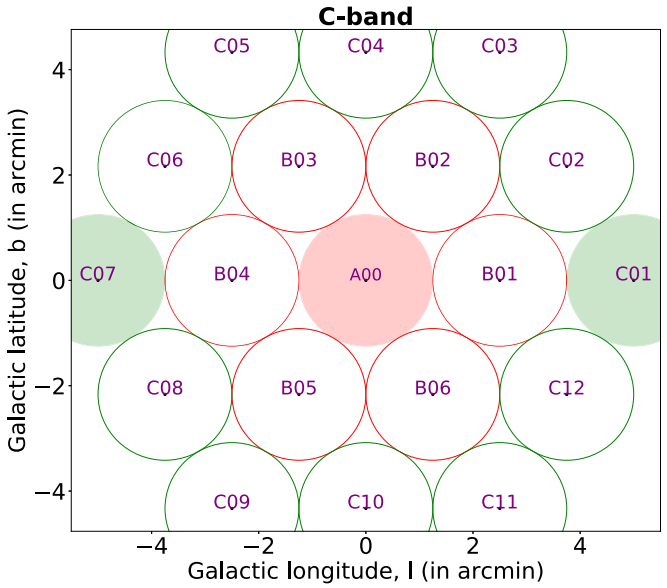

Figure 3. Pointings at *C* band for the BL GC survey with the GBT. The central pointing, labeled as A00 and shown with light red filled circle, indicates the region of deep pointing of the GC (0, 0) at *C* band. The rest of the pointings fully sample the $4' \times 4'$ GC bulge region. We highlight two pointings with green fill to demonstrate observation pairs with A00: A00-C01-C07-A00-C01-C07-A00-C01-C07. We should note that only for the A00, C01, and C07 pointings have we have the approach of switching between three pointings. For all the other pointings, we have utilized pairs of two faraway pointings to mimic standard ON-OFF observations.

to survey the GC bulge and the GC (0, 0). Here, the second beam will provide OFF-source pointing for deep and standard pointings. Since three bands are required to sample the full receiver bandwidth, 60 pointings will be used per band for the bulge and a total of three deep observations of the GC (0, 0) (see Figure 4(d)). The 180 pointings of 15 min each from the GC bulge and three pointings (4 GHz per pointing) of 3 h each for GC (0, 0) give a total observing time of 54 h.

Q Band (38.2–49.8 GHz) Like the Ka band, the *Q* band also has a dual-beam receiver, each dual-polarization (circular) at a fixed separation ($57\farcs8$ in the cross-elevation direction). The instantaneous bandwidth is 4 GHz. Thus, with the BLDB, we will record data from both beams. The offset beam will be used to increase the sky coverage and provide OFF-source pointings for the GC bulge and the GC (0, 0). The $2'$ region of the GC bulge is divided into 90 pointings (see Figure 4(e)). We plan to spend 15 min for bulge pointings and 3 h for the deep observations of the GC (0, 0) region. Since two bands are required to sample the full receiver bandwidth, 90×2 bulge pointings and 3×2 deep observations provide us a total of 51 h of observation.

W band (67–93 GHz) The *W*-band receiver also has two beams, each dual-polarization (linear) at a fixed separation ($286''$ in the cross-elevation direction). Similar to *Ka* and *Q* band, we will use the second beam to increase the sky coverage and obtain OFF-source pointings. We will sample a $1'$ region of the GC bulge with 37 pointings (see Figure 4(f)). We plan to spend the standard 15 min for bulge pointings and 2 h for the deep observations of the GC (0, 0) region. The band is split into four separate bands (67–74 GHz, 73–80 GHz, 79–86 GHz, and 85–93.3 GHz), only one of which can be used at a time. Thus, 36×4 pointings for the bulge along with 2×4 pointings for the GC (0, 0) will be completed in 44 h.

4. Observations

In this section, we discuss preliminary observations from the GBT (11.2 h) and Parkes (7.0 h). Table 3 includes a list of pointings and observing dates that are discussed in the following sections.

4.1. GBT

Here, we report observations on the GC carried out in five sessions between 2019 August 07 and 2019 September 11 using the *C*-band receiver at the GBT. As indicated in Section 3, these observations were conducted toward 19 pointings (see Figure 3) for three five-minute scans each. We also conducted deep observations of around 6.5 h toward the GC (0, 0), marked as pointing A00. We labeled the surrounding hexagon pointings as *B* and *C* (*D*, *E*, *F*, and *G* for higher bands), numbering the beams counterclockwise starting immediately to the right of A00. In order to eliminate false positives for the narrowband searches due to terrestrial RFI, we carried out observations in a sequence that allowed two HPBW separations between consecutive pointing centers. The shorter scans toward A00 were followed by two shorter scans of outer-ring pointings, i.e., C01 and C07. The other pointings were observed in the following pairs: B01–B04, B02–B05, B03–B06, C02–C04, C03–C05, C06–C08, C09–C11, and C10–C12 (see Figure 3). We also recorded noise-diode scans on the flux calibrators and a strong pulsar to measure our sensitivity and configuration during most sessions (see Table 3).

The observations, also listed in Table 3, were conducted using the BLDB. The BLDB provides a unique flexibility to capture and record baseband raw voltages across 12 GHz of bandwidth with 64 compute nodes at 32 bit resolution, making it one of the most powerful backends at the GBT. These compute nodes are clustered in eight banks, with each bank hosting eight compute nodes. We also have 10 storage nodes with a total recording capacity of 8.2 PB for long-term storage. For our observations, the BLDB repurposed the existing VEGAS backend (Versatile Greenbank Astronomical Spectrometer; Prestage et al. 2015) to tap into the GBT analog downconversion streams with four 1500 MHz wide tunable passbands covering the entire *C*-band receiver frequency response, spanning 3.9–8.0 GHz. This interface provided coarsely channelized raw digitized voltages into 512 polyphase channels—with 2.97 MHz of channel resolution. The recordings of these raw voltages are carried out across an array of 32 compute nodes in four banks, with each compute node configured to record 187.5 MHz of the bandwidth. We configured our backend with central on-sky frequencies of 4312.5, 5437.5, 6562.5, and 7687.5 MHz for the four overlapping bands. These frequencies were chosen to allow signal at the edges of each passband's intermediate frequency filter to overlap the adjacent passband by 2×187.5 MHz, allowing overlap of two compute nodes between banks. This resulted in a total 4875.0 MHz of bandwidth overlapping the entire *C*-band receiver instantaneous bandwidth of 4100 MHz.

4.2. Parkes

We report observations of the GC carried out in four sessions between 2020 April 10 and 2020 April 25 using the UWL receiver at the Parkes telescope. We conducted observations toward 14 pointings, with three scans each for 10 minutes per scan (Figure 2). We observed the GC (0, 0), labeled as A1, and

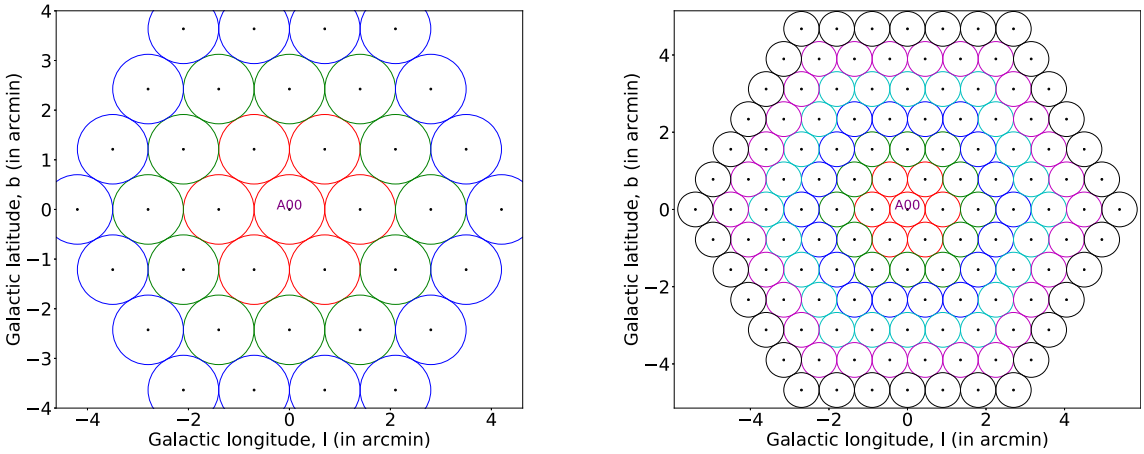

(a) X-band

(b) Ku-band

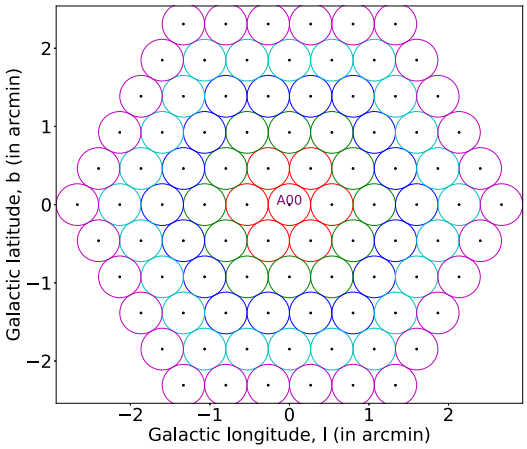

(c) KFPA-band

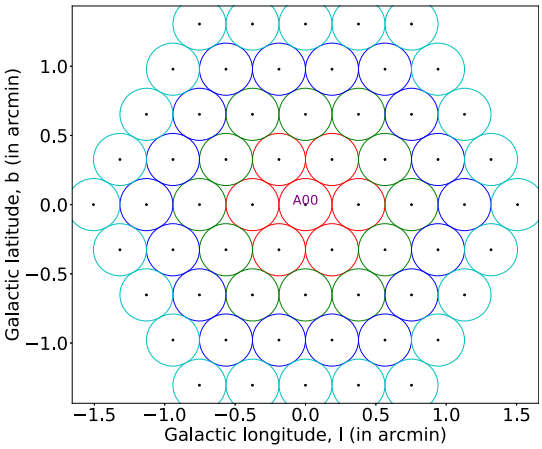

(d) Ka-band

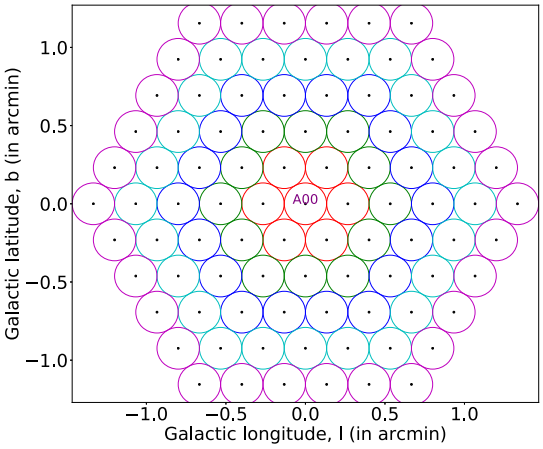

(e) Q-band

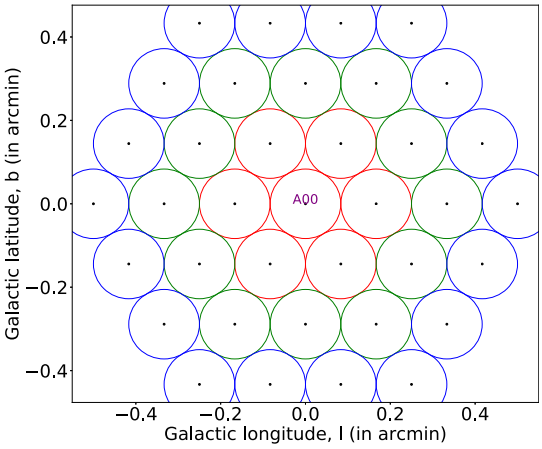

(f) W-band

Figure 4. GBT pointings for *X* to *W* band. The middle pointing, labeled as A00, indicates deep integrations of the GC (0, 0). The rest of the beams are fully sampled at a fixed integration time around the GC.

its immediate surrounding region (A2–A7), using OFF pointings one beamwidth away (B1–B7) to avoid detecting false positives as described above in Section 4.1. The pairs for our 14 pointings are as follows: [A1–B1], [A2–B2], ..., and [A7–B7]. The calibrators and test pulsars used to verify system integrity for most sessions can be found in Table 3.

Observations were recorded on the 26 BL compute nodes that comprise the BL data recorder system at Parkes. Price et al. (2018)

Table 3
Details of the Observations Analyzed in This Paper from the GBT and Parkes

GBT					
Date	Start MJD	Fields	Calibrator	Test pulsars	Total On-source Time (min)
2019–08–07	58702.20313657	A00,C01,C07	3C295	B0355+54, J1744–1134	40
2019–08–09	58704.99252314	A00,B01–B06,C01–C12	3C286	B1133+16, J1744–1134	285
2019–09–07	58733.98109953	A00	3C286	B2021+51	28
2019–09–08	58734.95761574	A00	…	…	60
2019–09–11	58737.95781249	A00	3C286	B2021+51	258
Parkes					
Date	Start MJD	Fields	Calibrator	Test pulsars	Total On-source Time (min)
2020–04–10	58949.58363425	A1, B1	…	…	60
2020–04–29	58968.61862268	A2, B2	0407–658	J1141–6545	60
2020–04–23	58962.55708333	A3, B3, A4, B4	1613–586	J1141–6545	120
2020–04–24/25	58963.56557870	A5, B5, A6, B6, A7, B7	0407–658	J1141–6545	180

Note. Columns list observing date, start time of the session, observed fields, calibrator, test pulsar, and total observing time for each session, respectively.

Table 4
Summary of Data Products Produced from the Standard BL Reduction Pipeline and Various Signal Types Possible to Search

Data Product	Frequency Resolution	Temporal Resolution	Possible Signal Searches
High-spectral resolution	∼3 Hz	∼18 s	**Narrowband drifting signals**
Mid-spectral resolution	∼3 kHz	∼1 s	Spectral line, wideband pulses from ETI
Mid-temporal resolution	∼350 kHz	∼349 μs	**Natural and artificially dispersed transients, pulsars, and FRBs**
High-temporal resolution[a]	∼91 kHz	∼43 μs	Wideband pulses from ETIs, pulsars, MSPs, and FRBs

Note. Signal searches that have already been carried out and discussed in this paper are marked with boldfaced text. All these data products from our survey will be publicly available for the community.
[a] These data products were only produced for the GBT.

provide a detailed summary of the BL data recorder and storage systems at Parkes. As mentioned previously, for these observations, we used the UWL receiver (Hobbs et al. 2020). The UWL digital systems digitize incoming voltages from the receiver at 16 bit resolution (for each pole), channelize the data streams into 26 coarse channels of width 128 MHz, and then output over high-speed Ethernet (total data rate ∼213 Gb s^{-1}). The BL data recorder (Price et al. 2018) captures these data (one 128 MHz sub-band per compute node) and produces spectral products as 32 bit floats (see Table 4). Copies of the data are also sent (via Ethernet multicast) to the primary telescope digital processor, Medusa (Hobbs et al. 2020).

4.3. Data Products

The BL standard reduction pipeline at both the facilities reduces the collected raw-voltage data products into various temporal and spectral resolution products for offline processing. A detailed summary of this BL reduction pipeline and discussion on various products is provided by Lebofsky et al. (2019). These formats are shown in Table 4. As discussed in Section 5.2, the GC region has a large electron density, which is likely to induce large dispersion and scattering for any putative transient signals. At lower frequencies, i.e., lower than 4 GHz with Parkes, these effects are dominating (with also increased noise temperature from the GC) and thus do not allow sensitive searches for transient signals. Therefore, in this paper, we only searched for transient signals (naturally and artificially dispersed) above 4 GHz with the GBT. Moreover, at the GBT, we also produced further high-temporal-resolution products that will be useful for the community to search for pulsars and MSPs above 4 GHz. We plan to publicly release all of our data collected from these observations via the Breakthrough Listen Open Data Portal[17].

5. Analysis

In this section, we discuss our search for two different classes of signals using the data collected from the Parkes with the UWL and with the GBT using the *C*-band receiver.

5.1. Narrowband Drifting Signal Searches

Narrowband signals have been proposed to be prime candidates for a deliberately transmitted beacon across large interstellar distances (Cocconi & Morrison 1959). We will not discuss the merit of such signals any further here, and instead refer to the earlier literature (see Tarter 2003 for a review). Due to the relative velocity between the transmitter and observer, such narrowband signals exhibit Doppler drifting across the observed band. If the narrowband signal at a fixed frequency is originating from a rotating object, the nonlinear velocity difference will cause the observed frequency of this signal to change nonlinearly. However, for shorter observing lengths, we can approximate such Doppler drifting as a linear chirp. We used turboSETI (Enriquez et al. 2017) to search for such linearly chirped narrowband signals from the high-spectral resolution data products. Here, we used chunks of 2.9 MHz of zero-drift time-summed spectrum to determine the standard deviation (σ). We used a drift rate search in the range of

[17] https://breakthroughinitiatives.org/opendatasearch

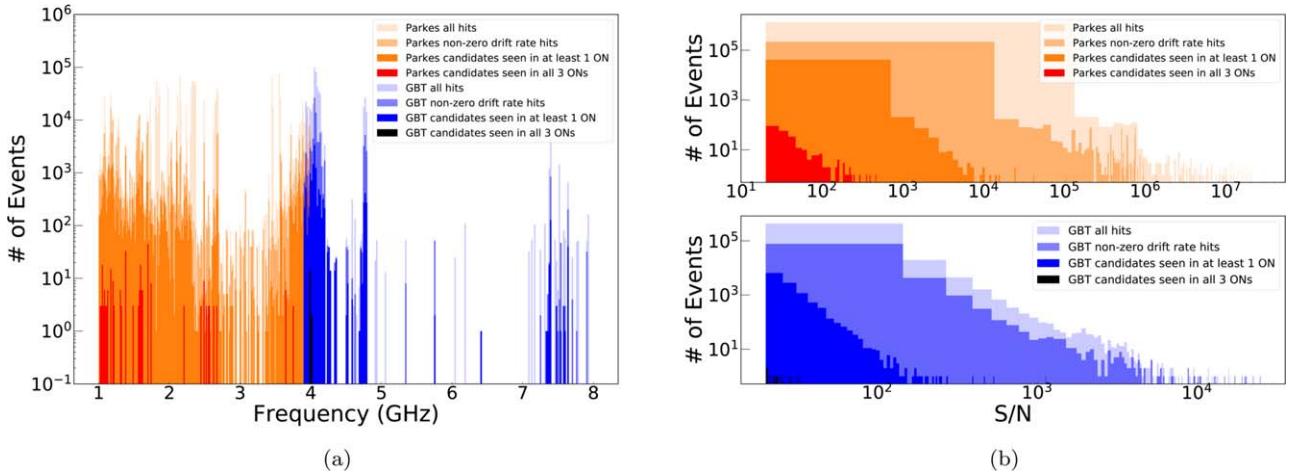

Figure 5. Distribution of "hits" obtained from the narrowband drifting signal searches conducted across 1 to 8 GHz as a part of the BL–GC survey. Left: Histogram shows the distribution of frequencies for all events detected in the GBT *C*-band and Parkes UWL data analyzed in this paper. Right: Histogram of S/N for the same events. We label these as "all hits," where we use 200 bins for frequency, 50 bins for drift rate, and 200 bins for S/N. Hits shown in lighter to darker orange are from Parkes, while hits shown in lighter to darker blue represents hits from the GBT for various filter cuts. For the frequency distribution of hits, the number of bins and their widths chosen are kept constant across Parkes and GBT data. However, because we only place a minimum threshold for S/N of 20, and there is no maximum limit, the width of the bins for S/N histogram is not restrained by a set maximum bound, but rather by the maximum value found within each filter. The final filter 3 hits are depicted by red bins for Parkes and black bins for GBT.

$\pm 4\,\mathrm{Hz\,s^{-1}}$ with 860 and 1720 steps for the GBT and Parkes telescopes, respectively. For each trial drift rate step, we produced a time-averaged high-spectral resolution dechirp spectrum. Fine channels from this 2.9 MHz chunk that were found to be above 20σ were identified as narrowband drifting signals, or "hits".

Such a range is sufficient to detect drifting introduced by any transmitter located on typical Earth-sized planets, including highly eccentric near-Earth objects (Sheikh et al. 2019). Sheikh et al. (2019) recommend that ideally drift rates in a range of $\pm 200\,\mathrm{Hz\,s^{-1}}$ should be used to search for such narrowband signals. This range covers observed drift rates from transmitters possibly located on numerous exotic objects such as gaseous planets and planets in highly eccentric obits. However, because searching through such a wide range of drift rates is computationally expensive, here we limit our drift rate search in the range of $\pm 4\,\mathrm{Hz\,s^{-1}}$, with the caveat that this is by no means a full search of all possible narrowband drifting signals contained in all the observations analyzed in this paper. For example, ongoing efforts to improve our narrowband searching code, turboSETI, have led us to find an improvement in sensitivity that will be tackled in future papers. Due to our specific frequency and time resolution of high-spectral resolution products, signals with higher drift rates will spread across multiple nearby channels within a single spectra, incurring loss in sensitivity equivalent to $1/N$, where N is the number of frequency channels over which a single signal is spread (see Margot et al. 2021 for a detailed discussion). However, it is possible to improve sensitivity by a factor of $\sqrt{N}$ for such high drifting signals by adding adjacent frequency bins or by using a varying-width moving boxcar (Price et al. 2020).

Using the search parameters listed in Table 5, we obtained a list of hits for each ON-OFF pair, as defined in Table 7, where each pair consists of a total of six observations—three ON and three OFF. We defined a "hit" as a single strong narrowband signal in an observation that is a fine channel above the set threshold. We found a total of 1,354,519 and 463,068 raw hits from Parkes and GBT observations, respectively. This hit density is relatively lower compared to the hit density obtained at *L* band from Price et al. (2020), as *C* band is relatively cleaner from interference and we have used a relatively higher threshold of 20σ. The distribution of these hits in frequency, S/N, and drift rate are shown in Figures 5(a), 5(b), and 6(a), respectively. Due to relatively lower observing frequencies with Parkes, we observed around double the number of total candidates with a roughly similar length of observations. We removed all the hits with a zero-drift rate, to eliminate as much RFI as possible, since any narrowband signals deliberately transmitted by ETIs would likely have some Doppler drift due to the relative velocity differences between the transmitter and the receiver. All the remaining hits, a total of 304,658 candidates combined from Parkes and GBT, are shown in Figures 5 and 6 as nonzero-drift-rate hits.

Table 5
Narrowband Search Parameters for the BL GC Survey

Parameter	Range
S/N_{min} threshold	20
Drift rate search	$\pm 4\,\mathrm{Hz\,s^{-1}}$
GBT frequency range	3.9–8 GHz
GBT trial drift rates	**860 steps**
Parkes frequency range	1–4 GHz
Parkes trial drift rates	**1720 steps**
Filter 2	Candidates seen in at least one ON and no OFFs
Filter 3	Candidates seen in all three ONs and no OFFs

After collating hits from the three ON-OFF pairs, we remove any hits for which at least one of the OFF observations has a hit in the range

$$\nu_{\mathrm{bound,OFF}} = \nu \pm |\dot{\nu}| \times 2(\Delta T). \quad (1)$$

Here, ν is the detected frequency of the hit, $\dot{\nu}$ is the maximum drift rate, and ΔT is the length of observations. Any remaining hits were considered an event, where we defined an "event" as a strong narrowband signal that was associated with a hit in at least one ON observation and no OFF observations. We defined these as "filter 2" events, which totaled to 53,702

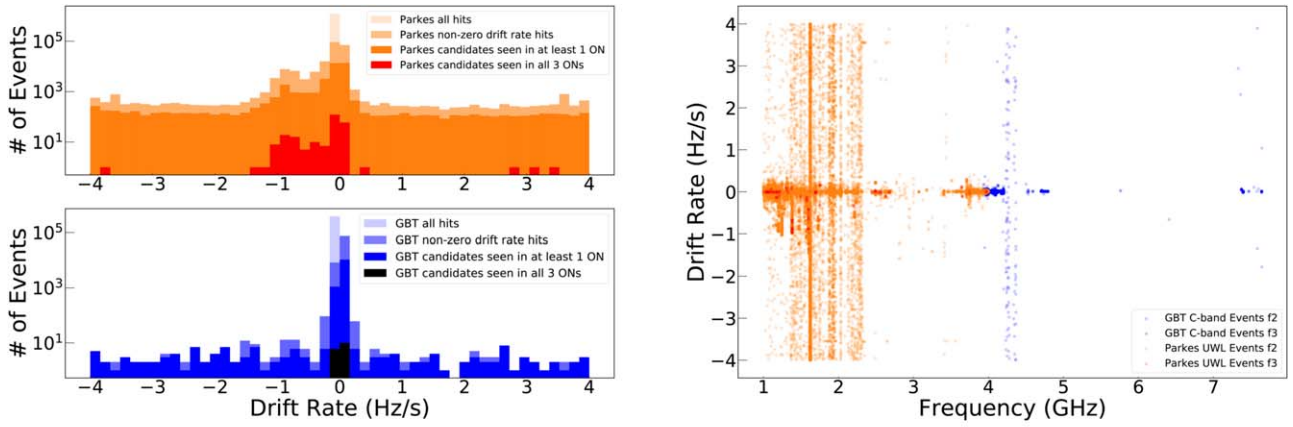

Figure 6. Distribution of "hits" obtained from the narrowband drifting signal searches conducted across 1 to 8 GHz as a part of the BL–GC survey. Left: Histogram shows the distribution of drift rates for all events detected in the GBT *C*-band and Parkes UWL data analyzed in this paper. Right: The scatter plot shows the distribution of drift rates across frequencies for the same events. The color labeling is similar to Figure 5.

candidates combined from Parkes and GBT, and they are shown in Figures 5 and 6. Finally, we filtered out hits by removing all those that did not appear in all three ON observations and did appear in any OFF observation. We defined them as "filter 3" events, which totaled to only 249 candidates. These are also shown in Figures 5 and 6.

We plotted all of our event candidates for both filter 2 and 3, which totaled to around 5.4×10^4 candidates, and vetted them by visual inspection. Any strong narrowband signals would appear in all three of the ON observations but none of the OFF observations. Table 7 shows the number of event candidates found for each ON source within each pair for both filter 2 and 3. We ran this process for each pair of observations: 14 Parkes UWL pointings and 19 GBT *C*-band pointings. Because the OFF observation for each ON observation is strategically placed inside the range of all our pointings, we are able to use this to our advantage by easily making double usage of each observation pair. For example, for the pair B01–B04 in *C* band, we can run turboSETI twice and look for narrowband drifting signals in two different areas: once using B01 as the ON source, and a second time using B04 as the ON source.

It is important to note that all of our pairs have a total of six observations; however, due to a split in our observation session for the GBT data, we only use four observations total (or two per pointing) for the pairs C07-A00 and C10-C12. Thus, an excess in the number of candidates for these pointings can be seen in Table 7. The rest of the pointings with high numbers of events are attributed to the large amount of RFI found in our data, as can be seen in 6(b), where many events were found to have drift rates close to zero. We did come across a few interesting Doppler-drifting candidates within this analysis; however, most of them can be attributed to RFI, since they appear in at least one of the OFF observations. Some examples of such interesting candidates are shown in Figure 7. Further details on these candidates are discussed in Section 6.1.

5.2. Transient Search

As suggested in Section 1.1, ETI inhabiting the Galactic Center region might transmit powerful artificially dispersed broadband pulses from an isotropic and/or a rotating beam transmitting all across the Galaxy as a beacon. This would require a similar amount of energy as the isotropic narrowband transmitter we searched for in the previous section. Any broadband signal passing through the interstellar medium experiences dispersion delay Δt due to the free electrons, at the observed frequency of ν compared to the infinite frequency as

$$\Delta t(DM, \nu) \propto \frac{DM}{\nu^2}. \quad (2)$$

Here, we can express the arrival time (Δt) and corresponding observed frequency (ν) in quadrants ($\pm\Delta t$, $\pm\nu$), also shown in Figure 8. It should be noted that the negative time and negative frequency only represent relative values for our given observation band in terms of respective channel and time sample indexes. For example, a signal with the noted arrival time of $\Delta t = -1$ is only in reference to arrival at $\Delta t = 0$ for a signal without any (artificial) dispersion delay. Here, the quadrant 1 (i.e., $+\Delta t$ and $+\nu$) transient signals are the ones that we refer to as naturally dispersed pulses, which are known to originate due to astrophysical transients such as FRB-like magnetars near the GC. An advanced communicating ETI civilization might choose to artificially disperse a broadband pulse that is not known to occur in nature. These other three classes of transient signals, located in the remaining three quadrants, are nonphysical and can be considered prime candidates for artificially dispersed broadband pulses that are easily distinguishable from the standard naturally dispersed signals. Here, we refer to these artificially dispersed signals as nT ($-\Delta t, +\nu$), nF ($+\Delta t, -\nu$), and nTnF ($-\Delta t, -\nu$). Such signals have been speculated as negative DM signals (von Korff 2010; Siemion et al. 2010; Harp et al. 2018; Li et al. 2020), but to the best of our knowledge, no comprehensive searches have ever been performed. Thus, our analysis is going to be the first of its kind to target such artificially dispersed transient signals.

In order to search these four types of broadband transient signals (shown in Figure 8), we have deployed a state-of-the-art GPU-accelerated and ML-assisted broadband signal detection pipeline named SPANDAK. This pipeline is an extension of the pipeline used for the detection of so far the highest known radio-frequency bursts from FRB (Gajjar et al. 2018). More

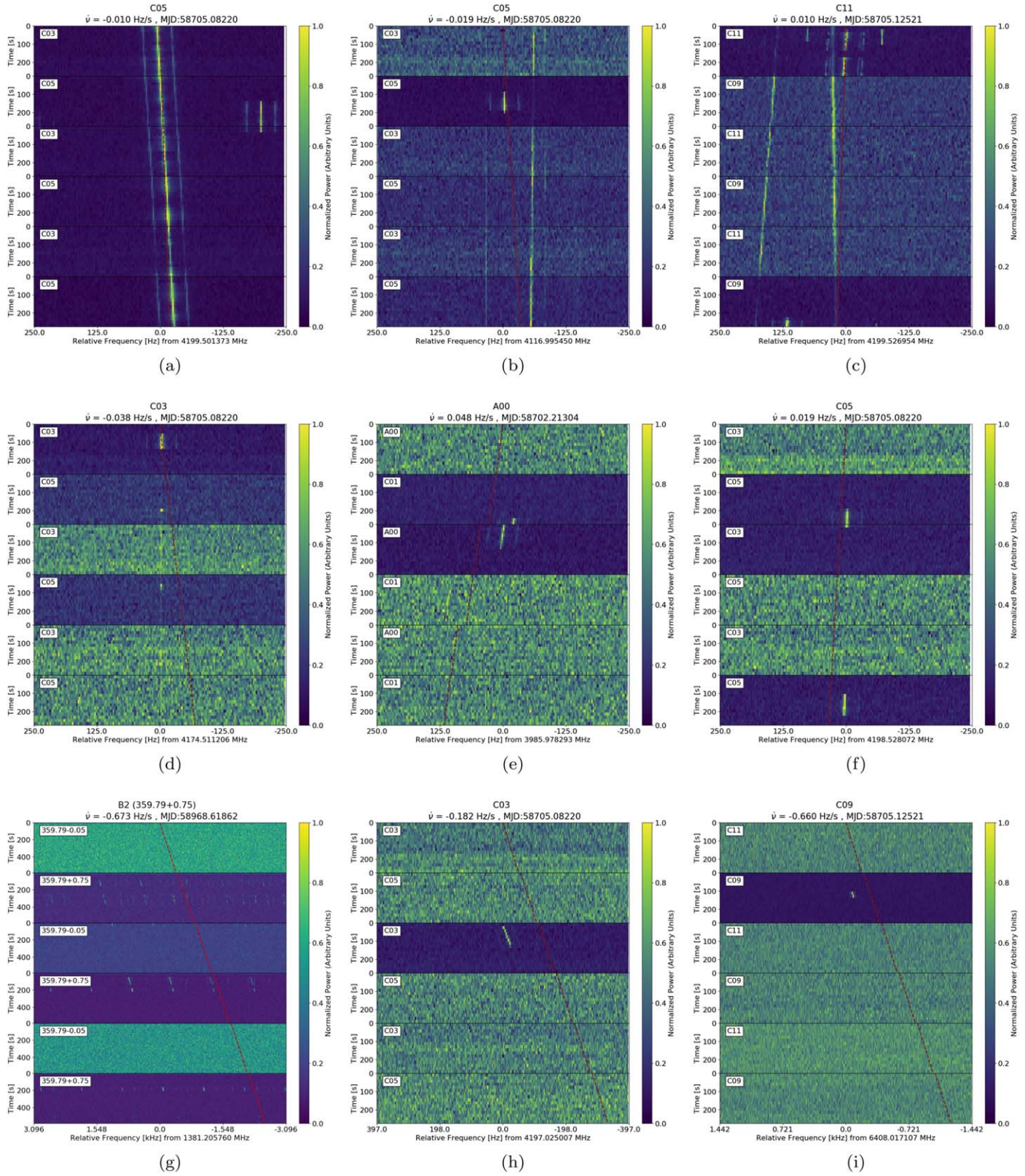

Figure 7. Examples of narrowband drifting signals found from the BL GC survey conducted across 1 to 8 GHz from Parkes and GBT. For each plot, dynamic spectra are shown for six observing ON-OFF pairs, with the top panel showing the first scan in the pair. The field name for the associated candidate is shown at the top of each plot. The center frequency of each event and measured drift rate are also listed at the bottom and top of each plot, respectively. The overlaid red dashed line shows the detected drift rate obtained from the first ON observation in which the signal first appears, with a slight offset in frequency for visualization; however, longer observations are needed for an exact drift rate. Apart from (g), all the examples are for candidates found from the GBT *C*-band observations.

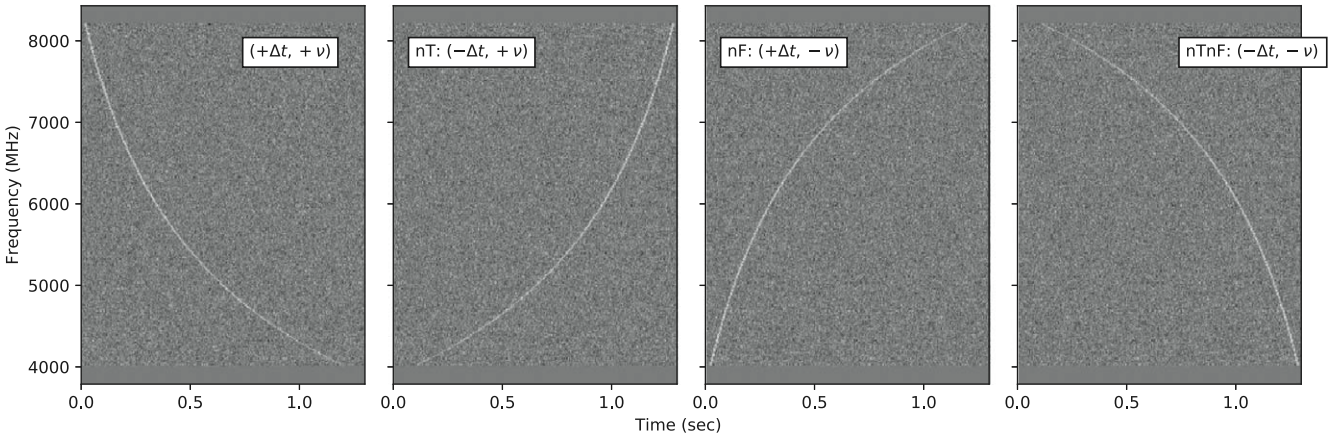

Figure 8. Four different types of transient signals we searched using the SPANDAK pipeline. Panels show dynamic spectra of dispersed pulses as a function of time and frequency. The leftmost panel shows the naturally dispersed pulse, occurring due to ionized interstellar medium. The other three panels are artificially dispersed pulses that are not known to occur in nature and can be used by ETIs as beacons.

Table 6
Transient Search Parameters for the BL GC Survey

Parameter	Range
DM (pc-cm^{-3})	−5000 to +5000
Maximum sensitivity loss due to DM steps	⩽15%
S/N_{min} threshold for pDM	6
S/N_{min} threshold for aDM	10
Width for pDM	0.38 to 97 ms **—with steps 0.38×2^n; with** $n \in [0,8]$
Width for aDM	0.7 to 194 ms **—with steps 0.7×2^n; with** $n \in [0,8]$

Note. Here, DM ranges refer to both natural and three types of artificial DMs.

details about the SPANDAK pipeline will be discussed in future publications (Gajjar et al. 2021 in preparation). As mentioned in Section 4.3, we only carried out these transient searches for our GBT data, since scattering and dispersion losses at lower frequencies render such searches less sensitive. Some of the search parameters for our GBT *C*-band transient search are listed in Table 6. For simplicity, natural DM candidates will be referred to as pDM (i.e., positive DM) candidates and three other types of transient signals—nT, nF, and nTnF—will collectively be referred to as artificial DM (i.e., aDM) candidates for the remainder of the discussion.

5.2.1. Positive DM Signal Searches

The GC region is likely to harbor an FRB-like magnetar population as suggested in Section 2.4.3. We searched for such transients using SPANDAK with the parameters listed in Table 6 for the mid-temporal resolution data product mentioned in Table 4. We first collated two nearby frequency channels and reduced the frequency resolution by a factor of 2 to get 6656 channels, as SPANDAK has a limitation of processing only up to 8k channels. We searched up to a DM of 5000 pc cm^{-3}. With our final temporal and frequency resolution products, the maximum channel smearing we will get for the highest DM is ∼0.38 ms. This is slightly higher than our sampling time for the data products (0.349 ms) used for this analysis. With this lower bound on the possible widths, we searched for bursts with widths up to 90 ms as mentioned in Table 6. We found a total of 4467 pDM candidates from all the pointings shown in Figure 3. A summary of the number of candidates observed from each of our *C*-band pointings are listed in Table 7. For each of the off-GC pointings (B and C rings) we observed roughly 80 to 100 candidates, which is consistent with our lower S/N_{min} threshold and interference environment. As can also be seen from Table 7, around 70% of the total candidates were found toward the GC(0,0) region. Figure 9 shows an example output plot from the SPANDAK pipeline. We visually inspected such plots for 4467 candidates and separated 667 candidates for further inspection. Figures 10(a) and 10(b) show the distribution of all observed candidates from one of the 30 minute scans and the distribution of 667 candidates from our entire observations with a first visual inspection cut. Out of these candidates, we identified 603 candidates from the Galactic center magnetar, SGR J1745-2900, as is clearly evident from Figure 10(b), with a large fraction of these candidates around the DM of 1778 pc cm^{-3}. The rest of the 63 candidates were viewed carefully by changing the number of sub-bands, number of time bins, and adjusting the detected DM to verify if the detected signal was real. Figure 11(a) shows one such example of an interesting candidate, which was later rejected. After this careful inspection, we were unable to verify the validity of these 63 remaining candidates and were unable to find any new pDM transient signals from our observations originating from astrophysical processes.

5.2.2. Artificial DM Signal Searches

The interstellar medium heavily impacts any signal being transmitted close to the GC. We refer to the Galactic density model from Yao et al. (2017), and considered that the largest DM one is likely to encounter toward the GC is on the order of 4000 pc cm^{-3}. It should be noted that the density model by Yao et al. (2017) may sometimes overpredict the DM in the plane of the Galaxy. Another Galactic density model by Cordes & Lazio (2002) (NE2001) may be more accurate; however, toward the GC, it also predicts a similar high DM. All three types of aDM signals are impacted differently. For example, signals with nT-aDM are indistinguishable from naturally dispersed signals if they are transmitted originally with an aDM less than the DM contribution from the Galaxy. Hence, when we refer to the DM limit for these signals, the original transmitted aDM would likely be ∼4000–9000 pc cm^{-3}. For nF-aDM and nTnF-DM

Table 7
Summary of BL Galactic Center Survey Conducted from the Parkes and GBT Telescopes Across 0.7 to 8 GHz

Parkes: 1.0 to 4.0 GHz									
Pair	ON-source pointing	R.A. (h:m:s)	Decl. (d:m:s)	l (deg)	b (deg)	f2 Events	f3 Events		
A1-B1	A1	17:45:40.04	−29:00:28.10	359.94	−0.05	291	0		
	B1	17:42:34.15	−28:35:25.90	359.94	0.75	9,301	138		
A2-B2	A2	17:45:18.09	−29:08:19.17	359.79	−0.05	1,424	0		
	B2	17:42:12.06	−28:43:15.04	359.79	0.75	7,149	36		
A3-B3	A3	17:46:01.93	−28:52:36.81	0.10	−0.05	1,012	3		
	B3	17:42:56.19	−28:27:36.52	0.10	0.75	3,446	27		
A4-B4	A4	17:46:00.21	−29:08:32.63	359.87	−0.18	1,116	0		
	B4	17:42:54.00	−28:43:32.13	359.87	0.62	3,384	15		
A5-B5	A5	17:46:22.11	−29:00:41.14	0.02	−0.18	1,036	0		
	B5	17:43:16.04	−28:35:42.55	0.02	0.62	4,935	12		
A6-B6	B6	17:44:57.98	−29:00:14.25	359.87	0.09	786	0		
	B6	17:41:52.26	−28:35:08.43	359.87	0.88	2,436	9		
A7-B7	A7	17:45:19.92	−28:52:23.38	0.02	0.09	802	0		
	B7	17:42:14.35	−28:27:19.50	0.02	0.88	4,727	9		
GBT: 3.9 to 8 GHz									
Pair	ON-source pointing	R.A. (h:m:s)	Decl. (d:m:s)	l (deg)	b (deg)	f2 Events	f3 Events	pDM Candidates	aDM Candidates
A00-C01	A00	17:45:40.04	−29:00:28.10	359.944	−0.046	2	0	see below	see below
	C01	17:45:51.95	−28:56:11.99	0.028	−0.046	3,129	3	43	21
C07-A00	C07†	17:45:28.12	−29:04:44.14	359.861	−0.046	1,687	0	51	29
	A00†	17:45:40.04	−29:00:28.10	359.944	−0.046	1	0	see below	see below
B01-B04	B01	17:45:45.99	−28:58:20.05	359.986	−0.046	1	0	52	112
	B04	17:45:34.08	−29:02:36.13	359.906	−0.046	203	0	80	150
B02-B05	B02	17:45:34.57	−28:58:16.40	359.965	−0.010	75	0	113	240
	B05	17:45:45.52	−29:02:39.78	359.923	−0.082	53	0	84	140
B03-B06	B03	17:45:28.61	−29:00:24.42	359.923	−0.010	64	0	83	90
	B06	17:45:51.47	−29:00:31.72	359.965	−0.082	38	0	80	100
C02-C04	C02	17:45:40.52	−28:56:08.37	0.007	−0.010	271	0	73	55
	C04	17:45:23.14	−28:58:12.69	359.944	0.026	457	0	35	58
C03-C05	C03	17:45:29.10	−28:56:04.69	359.986	0.026	291	0	100	65
	C05	17:45:17.18	−29:00:20.67	359.903	0.026	2,038	0	86	27
C08-C06	C08	17:45:39.56	−29:04:47.83	359.882	−0.082	57	0	73	15
	C06	17:45:22.65	−29:02:32.42	359.882	−0.010	582	0	53	31
C11-C09	C11	17:46:02.90	−29:00:35.29	359.986	−0.118	1,605	0	51	23
	C09	17:45:51.00	−29:04:51.46	359.903	−0.118	118	0	46	81
C10-C12	C10†	17:45:56.95	−29:02:43.38	359.944	−0.118	282	16	51	20
	C12†	17:45:57.42	−28:58:23.65	0.007	−0.082	917	0	109	59
Deep	A00†	17:45:40.04	−29:00:28.10	359.944	−0.046	⋯	⋯	3190★	955★

Notes. The R.A., decl., and Galactic coordinates for each ON-source pointing are listed in columns 3–6. Columns 7 and 8 show the number of candidates detected by turboSETI for each ON source, for each filter as described in Section 5.1. The ON sources for which four observations were used instead of the standard six are labeled with a †; this only applies to our turboSETI analysis. The last two rows show the number of transient candidates found for both naturally (pDM) and artificially (aDM) dispersed signals. The transient analysis used all three five-minute-long observations per pointing, with the exception of A00, for which we included twelve thirty-minute-long searches as well. These values are labeled with a ★, and are combined candidates from these deep and shorter observations toward the A00 field. The broadband analysis was not extended to the fields observed from the Parkes telescope, due to excess scattering and channel smearing losses

types of signals, the dispersion due to interstellar medium heavily impacts their shape and would render them indistinguishable from interference. Thus, in order to recover their original aDM shape, we dedisperse all mid-time-resolution data products at the DM of 4000 pc cm^{-3} before searching for nF-aDM and nTnF-aDM bursts. With this dispersion, we had to collate frequency resolution by a factor of 4 (3k channels) compared to the original mid-temporal resolution products. Thus, due to further channel smearing, our minimum burst width will be on the order of 0.7 ms for artificial transients across 4 to 8 GHz.

For the aDM signal searches, we searched twice the maximum pulse widths compared to our pDM search as indicated in Table 6. We found a total 2276 candidates combined from all three different aDM types with an S/N_{min} cut of 10. Table 7 summarizes a number of candidates found from each of the pointings. Figure 10(b) shows a histogram of these candidates. From our initial inspection of SPANDAK plots (such as shown in Figure 9), we found 56 candidates for further inspection. Figures 11(b) and (c) show examples of two such interesting aDM candidates. Further discussions of these candidates are outlined in Section 6.1.

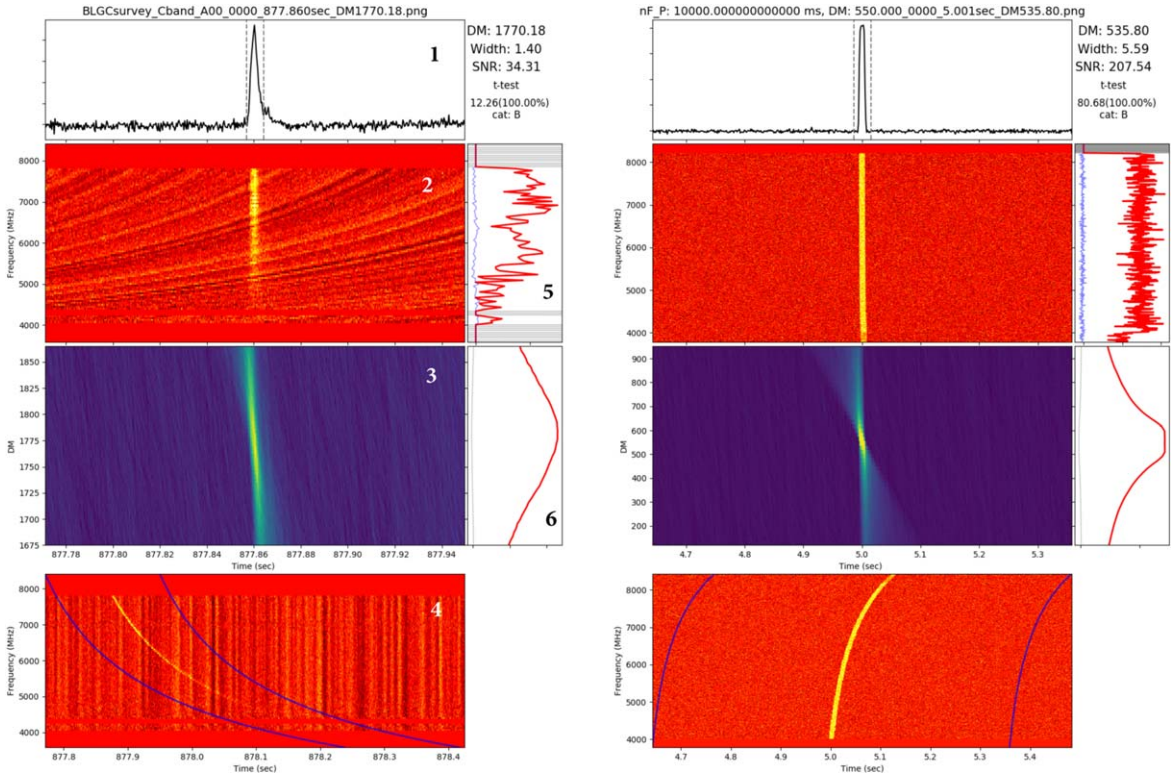

(a) (b)

Figure 9. Example plots from the SPANDAK pipeline. Left: A single pulse detected from SGR J1745–2900 from our observations of the GC (0, 0) across 3.9 to 8 GHz from the GBT. Panel 1 shows a dedispersed single pulse with an on-pulse region marked by two dotted lines along with the necessary diagnostic information next to it showing DM (pc cm^{-3}), S/N, and width of the detected candidate in milliseconds. Panel 2 shows dedispersed dynamic spectra showing a broadband pulse across 3.9 to 8 GHz with on-pulse and off-pulse spectra shown in red and gray lines in panel 5, respectively. Panel 3 shows the DM vs. time plot, with on-pulse DM vs. S/N shown in panel 6. Panel 4 shows the original data with the detected dispersed pulse along with two blue lines for visual guidance. Panels 1, 2, and 3 share the same time axis. The colors in all three panels are normalized intensities in arbitrary units. Right: A simulated pulse detected from the SPANDAK pipeline showing nF-aDM pulse.

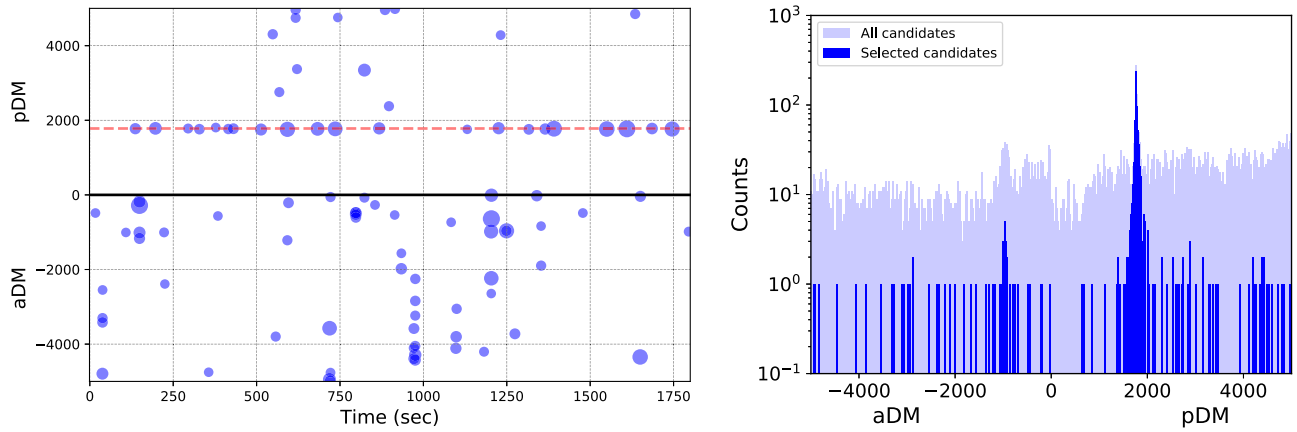

(a) (b)

Figure 10. Distribution of pDM (pc–cm^{-3}) and aDM (pc-cm^{-3}) candidates from the SPANDAK pipeline from the GBT *C*-band observations. Left: Distribution of pDM and aDM candidates from one of the 30 minute scans toward the A00 field. The size of the point represents the relative S/N. The red dotted line indicates the DM of 1778 pc cm^{-3}. Right: Histogram of all the detected candidates as a function of pDM and aDM from all fields. A clear peak near the DM of 1778 pc cm^{-3} is apparent due to large number of single pulses detected from SGR J1745–2900. For clarity, only candidates with S/N > 10 were used for both these plots.

6. Discussion

6.1. Candidate Signals from ETI

We carried out searches for two different types of beacons that are likely to originate from: (1) a transmitter placed near the GC, illuminating the entire Galaxy; and/or (2) any star in the lines of sight of our pointings toward the GC.

6.1.1. Narrowband Drifting Candidates

As mentioned earlier, we carried out three pairs of ON–OFF observations and compared narrowband drifting signals across ON and OFF pointings for all pairs. Some straightforward examples of candidates classified as RFI can be seen in Figure 7. A clear RFI signal can be seen in Figures (7(a)–(c)),

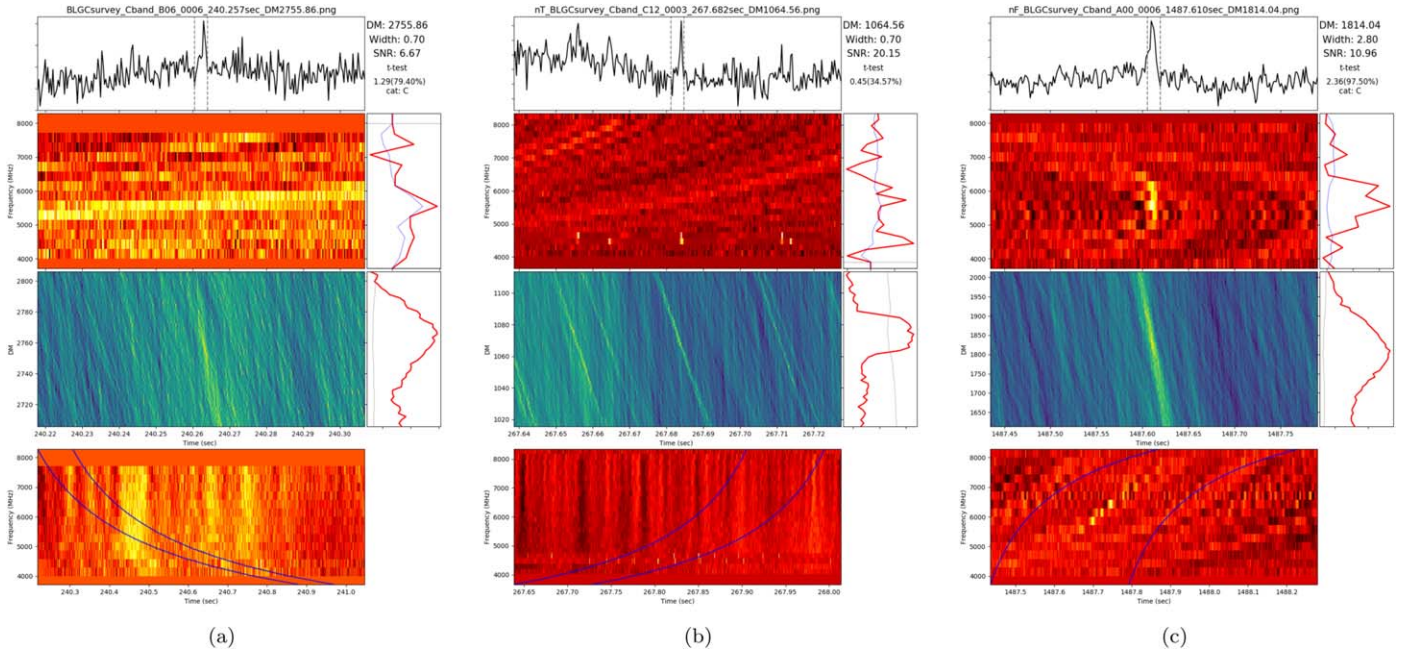

Figure 11. Tentative pDM and aDM candidates from the GC survey conducted across 3.9–8 GHz from the GBT found using the SPANDAK pipeline. Left: pDM candidate found toward B06 field at the DM of 2755 pc cm^{-3}. After careful examination, we were unable to verify the validity of this candidate. Center: One of the nT-aDM candidates found toward C12 field at the aDM of -1065 pc cm^{-3}. We detected several such candidates, as can be seen as a marginal excess in candidates around -1000 pc cm^{-3} in Figure 10 due to this peculiar interference Right: One of the nF-aDM candidates found toward the A00 field at an aDM of -1814 pc cm^{-3}.

where we see the signal appearing in all six observations. In these three examples, a clear and sometimes intermittent triplet pattern (central carrier with two sidebands) can be seen, which is likely to be a terrestrial communication signal. If the drift rate of this signal was significantly nonzero and was not present in the off scans, this would be an incredibly intriguing signal. Signals shown in Figures 7(a) and (c) also appear to have similar frequency (4199.5 MHz) despite coming from different pointings. A slightly dimmer RFI signal can also be seen in Figure 7(d) for ON and OFF observations. Such weaker signals are less likely to be detected above our S/N_{min} threshold and are likely to be rejected automatically without careful visual inspection. Examples shown in Figures 7(e) and (f) are interesting candidates where a signal is seen in one and two ON-source pointings, respectively. However, upon careful inspection it can be seen that the same signal is also visible at the beginning of the OFF pointing. Additionally, the drift rates of these signals are close to zero, and thus they are likely to originate from terrestrial sources.

Although most of the examples shown in Figure 7 were detected with the GBT data, an interesting example was found in the A2–B2 (359.79–0.05 & 359.79+0.75) pair with the Parkes UWL observations. Figure 7(g) shows several closely spaced strong narrowband drifting signals in the second, fourth, and sixth panels. This strong signal appears as a candidate event several times throughout our candidate list, both using filter 2 and 3 across a few other pointings. Since this is an interesting candidate passing our final filter 3, we carefully compared the detected frequency of the candidate against the satellite database and their transmission frequencies. Indeed, we find that the frequency at which these signals are found (1381 MHz) is also the frequency at which the GPS satellite Navstar transmits. Thus, due to its detection across other pointings and association of the detection frequency with a known satellite transmission, we are unable to consider this as a likely candidate of extraterrestrial origin. Nevertheless, it is a good depiction of what we expect a potential ETI signal to look like: nonzero drifting and appearing in all three ON observations but none of the OFF. The two remaining events from Figures 7(h) and 7(i) are the most interesting. The candidate shown in Figure 7(h) is found at 4.197 GHz, where a large concentration of hits are seen across other pointings as shown in Figure 5(a) and thus can still be rejected as RFI. However, the candidate shown in Figure 7(i) occurring at 6.408 GHz is unique and is seen only once in our entire set of observations (see Figure 5(a)). Since we did not find it to repeat during the other ON pointings, we still discard it as RFI due to some intermittent terrestrial source or coincidental passing of a low Earth orbit satellite across our beam during that single five-minute observation pointing toward C09. In summary, we did not find any strong evidence of narrowband drifting signals based on our criteria. Thus, we can reject the presence of strong beacons transmitting between 1 to 8 GHz with a 100% duty cycle located either at the GC or from other line-of-sight stars. However, we should point out that there are a few caveats on these constraints we obtained on the existence of such signals. For example, we only searched a small fraction of drift-rate parameter space (± 4 Hz s^{-1}) and with a reduced sensitivity toward higher drift rate (see Margot et al. 2021). Also, our detection pipeline may have an imperfect recovery rate and we might miss a strong signal in our data. We will address the completeness of our analysis pipeline in future publications (Perez et al. 2021 in prep).

6.1.2. Broadband Candidates

We carried out a search for three different types of aDM candidates for the first time. After eliminating candidates originating due to RFI, we shortlisted 56 candidates. We carefully further inspected these selected candidates by changing the number of frequency channels, number of bins,

and adjusting aDM. Most of these candidates appear to occur due to peculiar interference that aligns so as to mimic the aDM dispersion pattern. For example, in Figure 11(b), there is a comb of interference present between 4.2 to 4.4 GHz. These comb of narrow frequency interference coincidentally happens to align with the nT-aDM dispersion curve. Figure 11(c) shows another example of an nF-aDM candidate found toward the A00 field at an aDM of -1814 pc cm^{-3}. This candidate is likely due to interference at zero DM, which due to its limited spectral coverage, appears to partially follow the nF dispersion curve. Overall, we did not find any real artificially dispersed candidates originating from a likely transmitter placed at the GC or from stars close to the GC. Since we only dedisperse the data products to a DM of 4000 pc cm^{-3}, to compensate for their likely origin at the GC, with our current analysis we are unable to verify the existence of such signals transmitted from other stars along the line of sight toward the GC. In the future, we plan to dedisperse our data products at multiple DMs before searching aDM signals, to compensate for their Galactic dispersion and likely origin from line-of-sight stars spread across 8.2 kpc.

6.2. Number of Stars Surveyed

In Section 2, we highlighted that a line of sight toward the GC encounters the largest number of habitable stars compared to any other direction in the sky. In this section, we make an order-of-magnitude estimation of the number of stars surveyed based on the stellar number density (stars/pc^3) in the radial direction of our survey. Gowanlock et al. (2011) outlined various stellar number density models and found that the Carroll & Ostlie (2007) estimation of the number density profile appears to match the observed stellar density in the Solar neighborhood. This number density is represented as a function of radial distance from the GC, R, and vertical height from the Galactic midplane, Z, as

$$n(Z, R) = n_0\,(e^{-Z/Z_{\rm thin}} + 0.085e^{-Z/Z_{\rm thick}})e^{-R/h_R}\ \text{stars/pc}^3. \quad (3)$$

Here, n_0 is the normalization factor, given by Gowanlock et al. (2011) as 5.502 stars pc^{-3}. The constants $Z_{\rm thin} = 350$ pc, $Z_{\rm thick} = 1000$ pc, and $h_R = 2.25$ kpc are thin-disk scale height, thick-disk scale height, and radial scale, respectively. As can be seen, although stellar density falls off very quickly in the Z direction, for smaller angular scales, it can be considered to have constant stellar density. For example, at the distance of 8.5 kpc with our survey region of $4' \times 4'$, the diameter of the region probed would be around 10 pc, for which the number density reduces by only 2.5% (from 5.96 to 5.81 stars pc^{-3}). This is not a significant change; thus, we use the midplane density and take it as a constant for the Z scale height.

To calculate the total number of stars, we considered a cone in the Galactic midplane toward the GC with the Sun at the apex. The angle of the cone changes as a function of our observing frequencies and proposed target region. We considered stars up to a distance of 8.5 kpc from Earth—this includes the central Galactic bulge, which has the largest concentration of stars. For our current $4' \times 4'$ region, if we count the number of stars from Earth to the GC, we will encounter $\sim 6 \times 10^5$ total stars. This number will decrease as we go to higher frequencies with the GBT, due to our reduced survey regions (see Table 2). For our already conducted survey of the Parkes region, which covers two $30' \times 30'$ fields (see Figure 2), we estimated that we surveyed around 60 million stars. The large concentration of these total surveyed stars are likely to reside close to the GC region. As indicated in Figure 1, a large fraction of these stars, especially the ones that are closest to the GC, may host habitable planets, and thus our survey provides some of the best constraints on the two types of beacons from the large number of habitable systems. We should highlight that these are only order-of-magnitude estimates and gauging the exact numbers, especially for Parkes ($2^\circ \times 4^\circ$), is a nontrivial task due to the validity of our assumed stellar number density model and small angle approximations.

6.3. Survey Sensitivity

We have conducted searches for two different signal types, and limits can be placed on our detection sensitivity to both these signal types. For narrowband drifting signals, the minimum detectable flux can be given as

$$S_{\rm min,narrow} = \frac{S/N_{\rm min}}{\beta}\frac{S_{\rm sys}}{\delta\nu_t}\sqrt{\frac{\delta\nu}{n_p\tau_{\rm obs}}}. \quad (4)$$

Here, S_{sys} is the system equivalent flux density, $\tau_{\rm obs}$ represents integration time, n_p is the number of polarizations, and $\delta\nu_t$ and $\delta\nu$ are bandwidths of transmitted and received narrowband signals, respectively. For our survey, we assumed a transmitted bandwidth of 1 Hz[18]. $S/N_{\rm min}$ represents a desired threshold, and β is the *dechirping efficiency*. As mentioned in Section 5.1, due to our frequency ($\delta\nu \sim 3$ Hz) and temporal ($\delta t \sim 18$ s) resolutions, high drift rate signals get spread across multiple channels, which reduces our sensitivity. This dechirping efficiency can also be expressed as follows for our survey:

$$\beta = \begin{cases} 1 & |\dot{\nu}| \leqslant 0.16\ \text{Hz s}^{-1} \\ \dfrac{3}{|\dot{\nu}| \times 18} & |\dot{\nu}| > 0.16\ \text{Hz s}^{-1}. \end{cases} \quad (5)$$

Here, $\dot{\nu}$ is the trial drift rate under consideration. Our dechirping efficiency reaches its maximum for drift rates $\leqslant 0.16$ Hz s^{-1} and gradually declines beyond this limit. As mentioned in Section 5.1, future narrowband searches will improve this efficiency by collapsing nearby channels or by using a moving boxcar of corresponding width for the number of channels a given signal is likely to have spread across (Price et al. 2020).

For the broadband pDM and aDM transient signals, the minimum detectable flux can be expressed as

$$S_{\rm min,transient} = S/N_{\rm min}\frac{S_{\rm sys}\beta}{\sqrt{n_{\rm p}\ \Delta\tau_{\rm pulse}\ \Delta\nu}}. \quad (6)$$

Here, $\Delta\tau_{\rm pulse}$ is the pulse width of pDM and aDM candidates, $\Delta\nu$ is the total instantaneous bandwidth, and β is the loss due to digitization. For pDM candidates we used an $S/N_{\rm min}$ threshold of 6, and for aDM candidates we used an $S/N_{\rm min}$ threshold of 10. For simplicity, we considered scatter-independent pulse widths. A more accurate width estimation based on the scatter broadening and corresponding sensitivity limitation are discussed further in Section 6.6. For both the

[18] Interstellar scattering causes broadening of a narrow spectral line (Cordes & Lazio 1991). For transmitters near the Sun, the broadening is $\ll$1 Hz and thus unimportant, but the strong scattering toward the GC can make this a significant effect. Thus, it is likely that transmitter bandwidth will be larger, which will increase our sensitivity. For simplicity, however, we have assumed it to be 1 Hz.

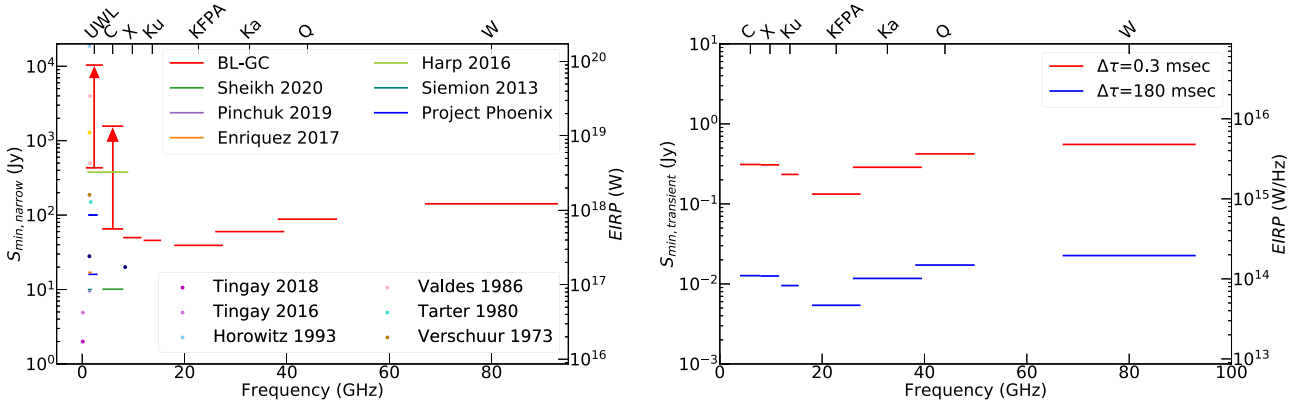

(a) (b)

Figure 12. Sensitivity for narrowband and broadband type signals across all observing frequencies for BL GC survey. Left: Minimum detectable flux for narrowband drifting signals as a function of frequency. For our current performed survey, the bounds at UWL and *C* band correspond to a changing dechirping efficiency, where the lower bound corresponds to the detection limit for drifting signals with $|\dot{\nu}| \leqslant 0.16$ Hz s^{-1} and the upper bound corresponds to the maximum drift rate (± 4 Hz s^{-1}) we included in the survey. A clear change in the sensitivity can be seen due to the combined effect from the increased $T_{\rm sys}$ at higher frequencies due to atmospheric contribution and the significant loss of sensitivity at lower frequencies due to excess $T_{\rm GC}$. We are also displaying similar limits from some of the well-known narrowband SETI surveys for comparison (Sheikh et al. 2020; Pinchuk et al. 2019; Enriquez et al. 2017; Tingay et al. 2016, 2018; Harp et al. 2016; Siemion et al. 2013; Horowitz & Sagan 1993; Valdes & Freitas 1986; Tarter et al. 1980; Verschuur 1973). Here, we have assumed a dechirping efficiency of 1 for all the other surveys, as calculating such efficiency based on the tools they have used is beyond the scope of this paper. Right: Minimum detectable flux limit for scatter-independent minimum and maximum pulse widths for broadband transient signals with both pDM and aDM types at an $S/N_{\rm min}$ threshold of 10. For both panels, the mirrored coordinate axes show the respective EIRP limits for putative transmitters residing at the distance of the GC.

signal types (narrowband and broadband), the S_{sys} can also be represented as

$$S_{\rm sys} = \frac{2k(T_{\rm sys} + T_{\rm GC})}{A_{\rm eff}}. \quad (7)$$

Here, $T_{\rm sys}$ is the system temperature at typical weather conditions[19], k is the Boltzmann constant, and $A_{\rm eff}$ is the effective aperture of the receiving antenna. The GC region contains a significant amount of background flux, especially with the lower-frequency receivers (up to Ku band). The excess noise contribution, which is expressed as $T_{\rm GC}$, will make a significant additional contribution to the $S_{\rm sys}$ (Johnston et al. 2006; Macquart et al. 2010), and needs to be included in the sensitivity calculations. Law et al. (2008) conducted a detailed continuum survey of the GC region using the GBT and computed a calibrated map of the region. Rajwade et al. (2017) used these measurements and derived the frequency dependence of this excess noise from the GC as

$$T_{\rm GC} = \frac{568}{\nu_{\rm GHz}^{1.13}}\ {\rm K}. \quad (8)$$

Here, $\nu_{\rm GHz}$ is the observing frequency. As can be seen, this will add a huge contribution to the system temperature at lower frequencies. For example, at 0.7 GHz from the UWL at Parkes, the expected noise contribution from the GC would be on the order of 800 K. Considering this contribution, our survey sensitivity is listed in Figure 12 for both narrow and broadband signals. As it can be seen, Ku and KFPA bands provide maximum sensitivity for both types of signals, with contribution from the GC dominating at lower frequency and contribution from the Earth's atmosphere dominating the T_{sys} at higher frequencies. Based on our minimum $S_{\rm min,narrow}$ and $S_{\rm min,broad}$ at various frequencies, we can calculate the corresponding Equivalent Isotropic Radiated Power (EIRP) at all our observing bands as

$${\rm EIRP}_{\rm GC;(narrow,\ broad)} = S_{\rm min;(narrow,\ broad)} \times 4\pi D_{GC}^2. \quad (9)$$

For transmitters at the distance of the GC, the minimum $\rm EIRP_{GC}$ are shown in Figure 12. It is evident that the minimum EIRP sensitivities of 3×10^{17} W and 4×10^{13} W/Hz are possible to achieve at the KFPA band for the narrowband and broadband transient signals, respectively. For our current survey with the GBT *C* band and Parkes-UWL, we estimate a minimum EIRP detection sensitivity of around 5×10^{17} W ($\gtrsim 10^{19}$ W for the signals with highest drift rates) and 4×10^{18} W ($\gtrsim 10^{20}$ W for the signals with highest drift rates) for the narrowband drifting signals, respectively. Similarly, for the broadband artificially dispersed signals from the GBT *C*-band survey, we estimate a minimum detectable EIRP of the order of 1×10^{14} W/Hz. It is clearly evident that broadband signals allow much better sensitivity to provide better constraints on the weaker signals if they are band-limited. However, since such signals are assumed to last for only a fraction of a second, we rely upon the repeatability of such signals, which is further discussed in Section 6.5.

6.4. Survey Figure of Merit

There have been several SETI surveys that have been conducted in the past six decades (Enriquez et al. 2017; Wright et al. 2018, and references therein). These surveys have primarily searched for narrowband drifting signals, and thus they can be compared with each other based on the total number of stars they surveyed (or total area of the sky covered), total bandwidth utilized, detection sensitivity, and other such parameters. For narrowband signals, the Drake figure of merit (DFM; Drake et al. 1984) has been computed by many previous SETI surveys. It can be expressed as

$${\rm DFM} = \frac{\Delta\nu\ \Omega}{S_{min,avg}^{\frac{3}{2}}}, \quad (10)$$

where Ω is the area of the sky surveyed, $S_{min,avg}$ is the minimum detectable flux average across all observing frequencies, and

[19] Table 2.2 in https://science.nrao.edu/facilities/gbt/observing/GBTog.pdf.

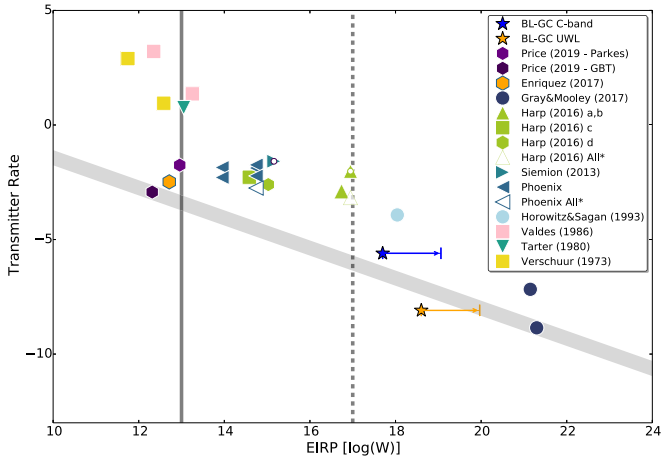

Figure 13. A comparison between the CWTFM vs. EIRP for some of the prominent SETI surveys compared to our BL-GC survey conducted at *C* band (blue star) and UWL (orange star) reported in this paper. For our surveys, we have shown the lower bound in EIRP limits that correspond to the dechirping efficiency and extend up to maximum drift rates searched at both bands. We have assumed a dechirping efficiency of 1 for all the other SETI surveys. The thick gray line shows the slope of the transmitter rate as a function of their EIRP power. The dotted line shows the total energy budget of a Kardashev Type I civilization, which is equivalent to the total solar power incident on Earth's surface. The solid vertical line shows the EIRP output of the Arecibo planetary radar.

$\Delta\nu$ is the total observing bandwidth. For our survey with the GBT across 3.9–8 GHz, we found the DFM to be $\sim 4 \times 10^{28}$ for the narrowband signals with drift rates $\leqslant 0.16\,\mathrm{Hz\,s^{-1}}$ and $\sim 4 \times 10^{26}$ for the highest drift rate considered for our survey. It should be noted that the DFM has a number of limitations as outlined by Enriquez et al. (2017) and Margot et al. (2021). For example, the DFM does not consider a range of drift rates and dechirping efficiencies, which heavily impacts $S_{min,avg}$ for a survey under consideration (Margot et al. 2021). Moreover, the DFM assumes a uniform distribution of ETI transmitters. For surveys like ours, where a large concentration of stars are likely to reside within our beam toward the GC, the DFM does not provide an accurate comparison. A better figure of merit is the Continuous Waveform Transmitter Rate (CWTFM), as introduced by Enriquez et al. (2017), which is also for narrowband signals and can be given as

$$CWTFM = \zeta_{\mathrm{AO}} \frac{EIRP}{N_{\mathrm{stars}}\,\nu_{\mathrm{frac}}}. \tag{11}$$

Here, ν_{frac} is the fractional bandwidth $\Delta\nu/\nu$, ζ_{AO} is the normalization factor such that CWTFM = 1 when the EIRP is equivalent to the EIRP of the Arecibo radio telescope's planetary radar ($\sim 10^{13}$ W), $\nu_{\mathrm{frac}} = 0.5$, and $N_{\mathrm{stars}} = 1000$. For our conducted survey, as discussed in Section 6.2, we can estimate the number of stars using the stellar density model and estimate the corresponding EIRP limits (see Section 6.3). We found that, for the UWL and *C* band, we surveyed around 60 million and 0.6 million stars, respectively. Figure 13 shows the measured CWTFM for our current *C*-band and UWL surveys compared with some of the prominent SETI surveys reported earlier. It is clearly evident that, with our current survey, we are already able to push the limit of transmitter-rate slope lower than what was obtained from previous SETI surveys. By extending this survey to other frequencies from the GBT and covering all the pointings from the Parkes telescopes, we are likely to push the CWFTM slope much lower and able to constrain the presence of technosignatures across a wide range of frequencies. Furthermore, Figure 12(a) shows a comparison of the sensitivity of narrowband signals of our survey with some of the prominent SETI surveys. As is clearly evident, no other survey has ever explored the frequency coverage we aim to search with our survey. Moreover, these comparisons are only carried out for narrowband drifting signals. Our survey is already the only survey to search for artificially dispersed signals that have never been explored, and thus it cannot be compared with any previous SETI surveys.

6.5. Limits on Repeatability of Broadband Signals from ETIs

We searched for three different types of artificially dispersed broadband transient bursts likely to originate from deliberately transmitted ETI beacons. In future work, we will provide a detailed discussion on harmonic searches for these broadband signals. In this section, we evaluate the repetition rate of these broadband bursts from our GC (0, 0) deep observations. Figure 14 shows one of the scenarios of repeating broadband signals originating from a rotating beam from an artificial beacon[20]. We can also infer different mechanisms that do not necessarily require a rotating beam but can still generate repeated bursts of similar nature. Such rotating beams of an artificial nature have been proposed earlier. For example, Benford et al. (2010a) suggested such a beacon situated at the GC would be the most energy-efficient way to signal the entire Galaxy. Shostak & Tarter (1985) have also considered narrowband signals originating from such a rotating beacon. We did not find any strong aDM candidates; thus, considering length and separation between all our observations, we can reject repetition of all three types of broadband signals. Table 3 lists all the observing dates and lengths of each of these observations. We arranged them on the time axis and then simulated pulse trains with a range of periods. We also adjusted the phase (or offset) of these bursts within the corresponding period under consideration. For each period, we calculated the number of instances of offset phases that would have allowed us to see at least one pulse. Here, we assumed that we are likely to detect a burst at every period. Figure 14 shows the probability of rejecting periods for such bursts. We can reject any mechanism that can regularly produce pulses across 3.9 to 8 GHz with a repetition period of around 4.3 hr with high accuracy (considering imperfect recovery rate of our search pipeline). For larger repetition periods up to 10 hr, we can reject such a mechanism with $\geqslant$50% probability, while for further large periods up to 100 hr, the rejection probability is marginal (<10%) from our observations. In the future, we plan to extend this analysis for narrowband signals and will also schedule our observations such as to allow sufficient epoch sampling to reject larger repeating periodicity with better significance. These limits are nontrivial to apply to astrophysical sources such as magnetars, which are not known to produce strong transient pulses during every rotation and their beam of emission is not necessarily likely to reside in the Z = 0 plane as we assumed for this analysis.

[20] Here, we are only considering rotation of an artificial beam transmitting pulses with aDM dispersion to illuminate the Galaxy. We are not considering sweeping of such an artificial beam to produce aDM bursts such as in the case of pulsars generating pDM bursts. Thus, we are not constrained by the beaming fraction of such a beam.

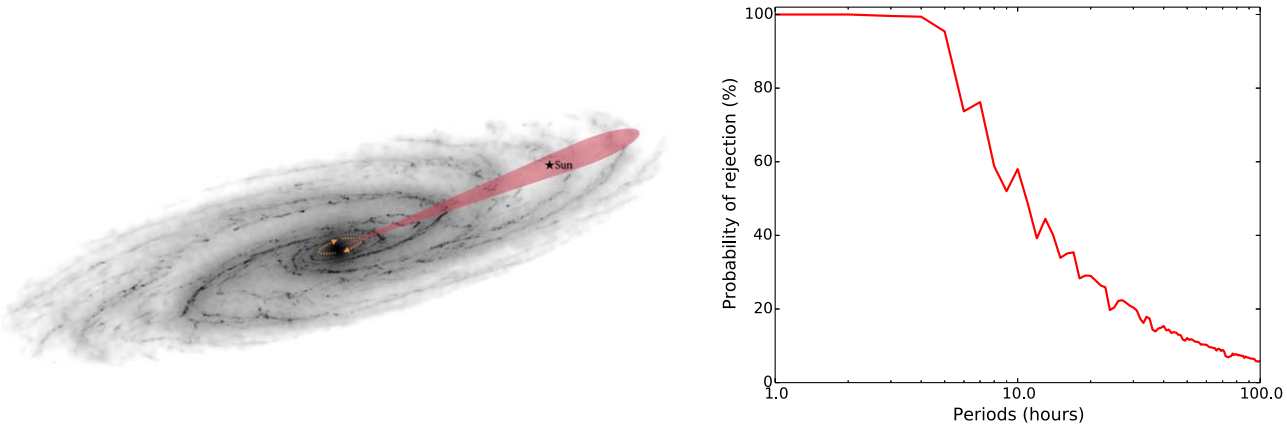

(a) (b)

Figure 14. Rejection of repeatability of broadband signals from our BL-GC survey conducted at *C* band. *Left:* Schematic sketch showing a rotating beam in Z = 0 plane from an artificial source located at the GC illuminating the entire Galaxy (sketch reproduced and modified by permission from Alex Pettitt, and originally from a simulation reported in Pettitt et al. 2015). *Right:* Probability of rejecting repeating bursts of natural or artificial origin for a range of periods.

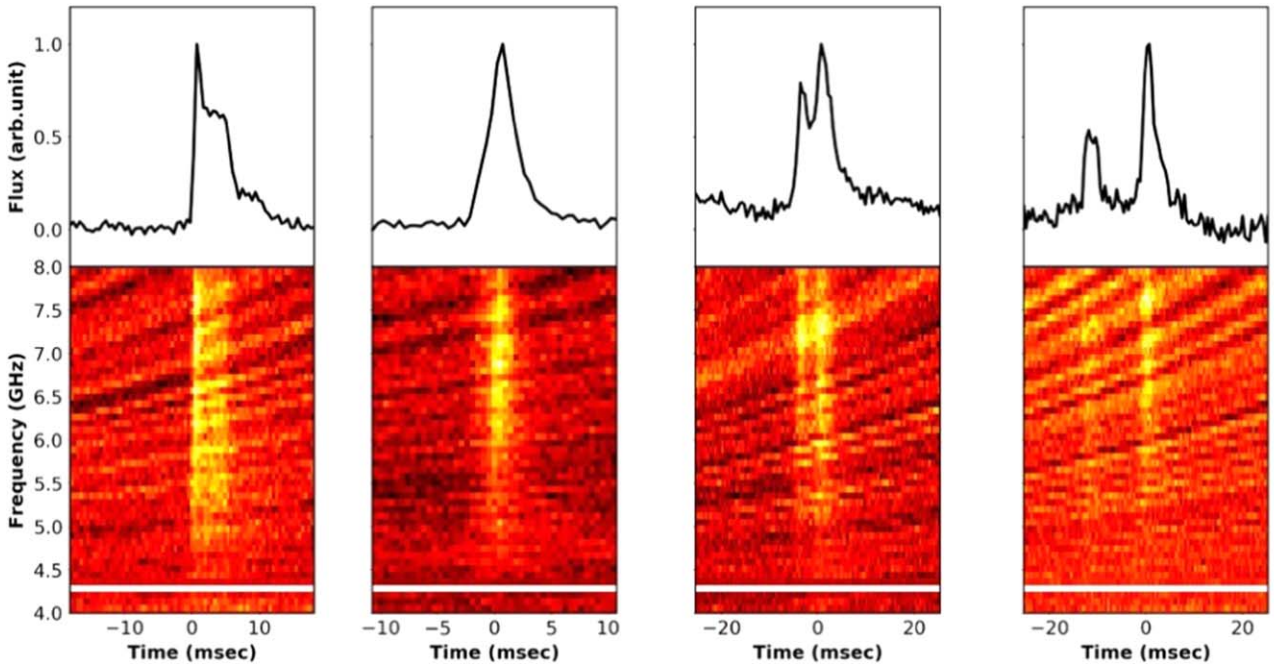

Figure 15. Four examples of different types of single pulses detected across 3.9 to 8.0 GHz from SGR J1745–2900 detected from the SPANDAK pipeline with the BL-GC survey.

6.6. SGR J1745–2900 and Constraints on Other Transients from Magnetars near the GC

We detected 603 single pulses from SGR J1745–2900 across 3.9 to 8.0 GHz with a total of 6.6 h of observations. These single pulses exhibit a wide variety of pulse shapes with single and multiple components. Figure 15 shows examples of four different types of single pulses seen from SGR J1745–2900 from our observations: a narrow single pulse with a scattering tail, a pulse with unresolved multiple components, and two well-resolved dual-component pulses. This is consistent with single pulses seen around similar frequencies by Pearlman et al. (2018) and Wharton et al. (2019). A detailed spectro-temporal analysis of these bursts is beyond the scope of this paper and will be reported in future publications. These observations are useful to constrain the presence of other radio magnetars at the GC producing transient bursts.

Scattering due to a relatively dense environment near the GC likely limits the detection of other transients. In order to estimate scatter-broadened pulse widths at our observed frequencies, we utilized a narrow single-peaked pulse from SGR J1745–2900 shown in Figure 15 for further analysis. Spitler et al. (2014) estimated that the scatter broadening (τ_d) from SGR J1745–2900 is on the order of 1.3 ± 0.2 sec at 1 GHz with a spectral index of $\alpha = -3.95 \pm 0.2$. Considering a similar spectral index, the expected τ_d will be $\sim$1.4 ms at 6 GHz. Measuring the observed τ_d is challenging, as suggested by Krishnakumar et al. (2017), due to the degeneracy of the unknown intrinsic pulse width and unresolved emission components. To model our underlying observed single pulse, we assumed a simple intrinsic single pulse with a Gaussian profile from the source, convolved with the $s(t) = e^{-t/\tau_d} U(t)$ for transmission through the ISM, where $U(t)$ is a step function

with $U(t) = 0$ for $t < 0$ and $U(t) = 1$ for $t \geqslant 0$. For the intrinsic pulse, we considered a pulse width of 1.8 ms reported from Pearlman et al. (2018) at 8.4 GHz, which is close to the highest end of our observed band. Similar techniques have been used by Krishnakumar et al. (2017) and Krishnakumar et al. (2019) to estimate τ_d. We found the $\tau_d \approx 4$ ms by fitting this model to the narrow pulse shown in Figure 15. This is slightly higher and not consistent with the spectral index of −3.8 reported earlier at lower frequencies by Spitler et al. (2014). Similar inconsistencies were also reported by Pearlman et al. (2018). It is also likely that the larger scatter broadening is due to an unresolved emission component at the trailing edge of the pulse.

The scatter broadening timescale found from the narrow SGR J1745–2900 burst can be utilized to place a limit on other FRB-like Galactic magnetars and millisecond pulsars (MSPs) located in a similar environment around the GC. We re-evaluated our minimum detection limit for the broadband signals calculated in Section 6.3. We find that, for our current survey across 3.9 to 8 GHz for transients, we were sensitive to bursts with peak flux density of around 68 mJy, which is equivalent to the peak luminosity of $\sim 10^{31}$ erg s^{-1} across our band for a source located at the GC. Although average flux densities of folded profiles of radio-loud magnetars are relatively lower, single pulses from them do exhibit bright emission. For example, XTE J1810–197, a known Galactic radio magnetar, was seen to produce bright transient radio pulses up to 42 GHz (Camilo et al. 2006). XTE J1810–197 showed many single pulses with a peak flux of $\gtrsim$10 Jy at 6.4 GHz, which corresponds to a peak luminosity of around 7×10^{31} erg s^{-1} across their 500 MHz band. Similarly, another radio-loud magnetar, PSR J1622–4950, is known to show bursts with a peak flux of around 16 Jy (Levin et al. 2010b), which corresponds to a peak luminosity of 5×10^{32} erg s^{-1}. This is an order of magnitude larger than our limit. Moreover, the recently detected FRB-like Galactic magnetar, SGR 1935 +2154, also exhibits a bright luminosity on the order of 10^{36} erg s^{-1} (The CHIME/FRB Collaboration et al. 2020), which is several orders of magnitude larger than our peak luminosity limit. Since our longest observing run was about 4.3 h (see Table 3), we can reject the presence of any transient signal with a typical burst-rate of $\geqslant$0.23 bursts h^{-1} at our radio luminosity limit. A few of the radio magnetars are known to produce transient radio bursts with much larger burst rates. For example, SGR J1745–2900 produced $\gtrsim$10 bursts hr^{-1}, as measured from our observations.

Our scatter-broadened limits are also important, as many different theories have been proposed to solve the *missing pulsar* problem. For example, the GC has been considered to favor MSP production (Bartels et al. 2016). As we found a scatter broadening timescale of ∼4 ms, any MSP signals with much smaller intrinsic pulse widths than normal pulsars are likely to get scattered and will therefore be undetectable up to our highest frequency of 8 GHz. Extension of our survey to higher frequencies would be ideal to search for other such MSP near the GC.

7. Conclusion

In this paper, by extending the habitability model of Gowanlock et al. (2011) to the inner 2.5 kpc region, we demonstrated that a line of sight toward the GC is likely to render the largest concentration and highest number density of habitable worlds. The GC region also provides an ideal Schelling point for advanced civilizations to place a powerful transmitter to efficiently send beacons across the entire Milky Way. Thus, the GC is one of the primary targets of the BL program (Isaacson et al. 2017). We outlined our survey strategy for the most comprehensive search for evidence of intelligent life ever conducted by utilizing a large fraction of the accessible radio window (0.7 to 93 GHz) from the GBT and Parkes telescopes. We compared the sensitivity of our survey to some of the prominent SETI surveys and demonstrated that our survey has remarkable sensitivity with a frequency span never before explored for SETI.

We have reported early results from our survey of the GC region across 1 to 8 GHz with around 11.2 and 7 h of observations from the GBT and Parkes telescopes, respectively. We carried out searches for standard narrowband drifting signals, along with, for the first time, three different types of broadband artificially dispersed transient signals (up to a DM of −5000 pc cm^{-3}) using our state-of-the-art GPU-accelerated tools. We did not find a strong beacon signal for any of these signal categories searched. However, our survey already placed a constraint on the existence of narrowband transmitters of $\lesssim$1 in 60 million stars toward the GC across 1 to 4 GHz with EIRP $>4 \times 10^{18}$ W (and $\geqslant 10^{20}$ W for the signals with the highest drift rates). We were also able to place meaningful constraints for the first time on the existence of narrowband and broadband transmitters in $\lesssim$1 in half-a-million stars across 3.9 to 8 GHz with EIRP $>5 \times 10^{17}$ W (and $\geqslant 10^{19}$ W for the highest-drift-rate signals) and 1×10^{14} W/Hz, respectively. With our deep targeted observations of the GC (0, 0), we were also able to reject the existence of periodic broadband beacons showing characteristic aDM dispersion patterns with periods $\leqslant$4.3 h with similar EIRPs.

We also searched for astrophysical transient signals from other radio-loud magnetars near the GC. We searched for broadband pulses up to a DM of 5000 pc cm^{-3} with pulse widths ranging from 0.3 to 90 ms with $S/N_{min} \geqslant 6$. We found 603 single pulses from SGR J1745–2900, and we determined a scatter broadening on the order of 4 ms from one of the narrow detected pulses. Based on the scatter-broadening timescale, we ruled out the likely existence of other transient sources with a luminosity limit of $\geqslant 10^{31}$ erg s^{-1} with a burst rate of $\geqslant$0.23 burst hr^{-1}. This is around the typical peak luminosity of other Galactic radio-loud magnetars.

We would like to thank the anonymous referee for a critical review of the paper and for suggesting several improvements to the manuscript. Breakthrough Listen is managed by the Breakthrough Initiatives, sponsored by the Breakthrough Prize Foundation. S.C., J.M.C., and A.S. acknowledge support from the National Science Foundation (AAG 1815242). V.G. thanks Alex Pettitt for giving us permission to use a sketch of the Milky Way. The Parkes radio telescope is part of the Australia Telescope National Facility, which is funded by the Australian Government for operation as a National Facility managed by CSIRO. The Green Bank Observatory is a facility of the National Science Foundation, operated under cooperative agreement by Associated Universities, Inc. We thank the staff at Parkes and Green Bank observatories for their operational support. We also thank all the frontline workers during this global pandemic and all the California firefighters for keeping most of us out of harm's way.

ORCID iDs

Vishal Gajjar https://orcid.org/0000-0002-8604-106X
Karen I. Perez https://orcid.org/0000-0002-6341-4548
Bryan Brzycki https://orcid.org/0000-0002-7461-107X
Shami Chatterjee https://orcid.org/0000-0002-2878-1502
James M. Cordes https://orcid.org/0000-0002-4049-1882
Steve Croft https://orcid.org/0000-0003-4823-129X
David DeBoer https://orcid.org/0000-0003-3197-2294
Michael Gowanlock https://orcid.org/0000-0002-0826-6204
Howard Isaacson https://orcid.org/0000-0002-0531-1073
Brian C. Lacki https://orcid.org/0000-0003-1515-4857
Matt Lebofsky https://orcid.org/0000-0002-7042-7566
Ian S. Morrison https://orcid.org/0000-0003-0833-0541
Cherry Ng https://orcid.org/0000-0002-3616-5160
Imke de Pater https://orcid.org/0000-0002-4278-3168
Danny C. Price https://orcid.org/0000-0003-2783-1608
Sofia Z. Sheikh https://orcid.org/0000-0001-7057-4999
Akshay Suresh https://orcid.org/0000-0002-5389-7806

References

Backus, P. R. & Project Phoenix Team 2004, BAAS, 36, 805
Bartels, R., Krishnamurthy, S., & Weniger, C. 2016, PhRvL, 116, 051102
Benford, G., Benford, J., & Benford, D. 2010a, AsBio, 10, 491
Benford, J., Benford, G., & Benford, D. 2010b, AsBio, 10, 475
Bochenek, C. D., Ravi, V., Belov, K. V., et al. 2020, Natur, 587, 59
Bower, G. C., Deller, A., Demorest, P., et al. 2014, ApJL, 780, L2
Bryson, S., Kunimoto, M., Kopparapu, R. K., et al. 2021, AJ, 161, 36
Brzycki, B., Siemion, A. P. V., Croft, S., et al. 2020, PASP, 132, 114501
Camilo, F., Ransom, S. M., Halpern, J. P., et al. 2006, Natur, 442, 892
Camilo, F., Ransom, S. M., Peñalver, J., et al. 2007, ApJ, 669, 561
Carroll, B. W., & Ostlie, D. A. 2007, An Introduction to Modern Astrophysics (Cambridge, MA: Addison-Wesley)
Carroll-Nellenback, J., Frank, A., Wright, J., & Scharf, C. 2019, AJ, 158, 117
Cocconi, G., & Morrison, P. 1959, Natur, 184, 844
Cole, T. W., & Ekers, R. D. 1979, PASAu, 3, 328
Comisso, L., & Asenjo, F. A. 2021, Phys. Rev. D, 103, 023014
Cordes, J. M., & Lazio, T. J. 1991, ApJ, 376, 123
Cordes, J. M., & Lazio, T. J. W. 1997, ApJ, 475, 557
Cordes, J. M., & Lazio, T. J. W. 2002, arXiv:astro-ph/0207156
Cordes, J. M., Lazio, J. W., & Sagan, C. 1997, ApJ, 487, 782
Degenaar, N., Reynolds, M. T., Miller, J. M., Kennea, J. A., & Wijnands, R. 2013, ATel, 5006, 1
Deneva, J. S., Cordes, J. M., & Lazio, T. J. W. 2009, ApJL, 702, L177
Dexter, J., & O'Leary, R. M. 2014, ApJ, 783, L7
Di Stefano, R., & Ray, A. 2016, ApJ, 827, 54
Drake, F., Wolfe, J. H., & Seeger, C. L. 1984, SETI Science Working Group Report, 2244
Dressing, C. D., & Charbonneau, D. 2015, ApJ, 807, 45
Eatough, R., Karuppusamy, R., Kramer, M., et al. 2013a, ATel, 5040
Eatough, R. P., Falcke, H., Karuppusamy, R., et al. 2013b, Natur, 501, 391
Enriquez, J. E., Siemion, A., Foster, G., et al. 2017, ApJ, 849, 104
Gajjar, V., Perez, K., Siemion, A., et al. 2020, ATel, 13575, 1
Gajjar, V., Siemion, A., Croft, S., et al. 2019, BAAS, 51, 223
Gajjar, V., Siemion, A. P. V., Price, D. C., et al. 2018, ApJ, 863, 2
Genzel, R., Eisenhauer, F., & Gillessen, S. 2010, RvMP, 82, 3121
Ghez, A. M., Salim, S., Weinberg, N. N., et al. 2008, ApJ, 689, 1044
Gowanlock, M. G., Patton, D. R., & McConnell, S. M. 2011, AsBio, 11, 855
Gravity Collaboration, Abuter, R., Amorim, A., et al. 2019, A&A, 625, L10
Hankins, T. H., & Eilek, J. A. 2007, ApJ, 670, 693
Harp, G. R., Ackermann, R. F., Astorga, A., et al. 2018, ApJ, 869, 66
Harp, G. R., Ackermann, R. F., Blair, S. K., et al. 2012, arXiv:1211.6470
Harp, G. R., Richards, J., Tarter, J. C., et al. 2016, AJ, 152, 181
Hobbs, G., Manchester, R. N., Dunning, A., et al. 2020, PASA, 37, e012
Horowitz, P., & Sagan, C. 1993, ApJ, 415, 218
Howell, S. B., Sobeck, C., Haas, M., et al. 2014, PASP, 126, 398
Isaacson, H., Siemion, A. P. V., Marcy, G. W., et al. 2017, PASP, 129, 054501
Jiménez-Torres, J. J., Pichardo, B., Lake, G., & Segura, A. 2013, AsBio, 13, 491
Johnston, S., Kramer, M., Lorimer, D. R., et al. 2006, MNRAS, 373, L6
Kennea, J. A., Krimm, H., Barthelmy, S., et al. 2013, ATel, 5009, 1
Krishnakumar, M. A., Joshi, B. C., & Manoharan, P. K. 2017, ApJ, 846, 104
Krishnakumar, M. A., Maan, Y., Joshi, B. C., & Manoharan, P. K. 2019, ApJ, 878, 130
Law, C. J., Yusef-Zadeh, F., Cotton, W. D., & Maddalena, R. J. 2008, ApJS, 177, 255
Lebofsky, M., Croft, S., Siemion, A. P. V., et al. 2019, PASP, 131, 124505
Levin, L., Bailes, M., Bates, S., et al. 2010a, ApJL, 721, L33
Levin, L., Bailes, M., Bates, S., et al. 2010b, ApJL, 721, L33
Li, D., Gajjar, V., Wang, P., et al. 2020, RAA, 20, 078
Lineweaver, C. H., Fenner, Y., & Gibson, B. K. 2004, Sci, 303, 59
Lipman, D., Isaacson, H., Siemion, A. P. V., et al. 2019, PASP, 131, 997
Liu, K., Wex, N., Kramer, M., Cordes, J. M., & Lazio, T. J. W. 2012, ApJ, 747, 1
MacMahon, D. H. E., Price, D. C., Lebofsky, M., et al. 2018, PASP, 130, 044502
Macquart, J.-P., Kanekar, N., Frail, D. A., & Ransom, S. M. 2010, ApJ, 715, 939
Margot, J.-L., Pinchuk, P., Geil, R., et al. 2021, AJ, 161, 55
Mori, K., Gotthelf, E. V., Zhang, S., et al. 2013, ApJL, 770, L23
Morrison, I. S., & Gowanlock, M. G. 2015, AsBio, 15, 683
Newman, W. I., & Sagan, C. 1981, Icar, 46, 293
Oliver, B. M., & Billingham, J. 1971,
Pearlman, A. B., Majid, W. A., Prince, T. A., Kocz, J., & Horiuchi, S. 2018, ApJ, 866, 160
Pettitt, A. R., Dobbs, C. L., Acreman, D. M., & Bate, M. R. 2015, MNRAS, 449, 3911
Pfahl, E., & Loeb, A. 2004, ApJ, 615, 253
Pinchuk, P., Margot, J.-L., Greenberg, A. H., et al. 2019, AJ, 157, 122
Prestage, R. M., Bloss, M., Brandt, J., et al. 2015, URSI-USNC Radio Science Meeting, 2015, 4
Price, D. C., Enriquez, J. E., Brzycki, B., et al. 2020, AJ, 159, 86
Price, D. C., MacMahon, D. H. E., Lebofsky, M., et al. 2018, PASA, 35, 213
Rajwade, K. M., Lorimer, D. R., & Anderson, L. D. 2017, MNRAS, 471, 730
Schelling, C. T. 1960, The Strategy of Conflict (Oxford: Oxford Univ. Press)
Sheikh, S. Z., Siemion, A., Enriquez, J. E., et al. 2020, AJ, 160, 29
Sheikh, S. Z., Wright, J. T., Siemion, A., & Enriquez, J. E. 2019, ApJ, 884, 14
Shostak, G., & Tarter, J. 1985, AcAau, 12, 369
Siemion, A., Korff, J. V., McMahon, P., et al. 2010, AcAau, 67, 1342
Siemion, A. P. V., Demorest, P., Korpela, E., et al. 2013, ApJ, 767, 94
Spitler, L. G., Lee, K. J., Eatough, R. P., et al. 2014, ApJL, 780, L3
Surnis, M., Joshi, B. C., Bagchi, M., et al. 2020a, ATel, 13777, 1
Surnis, M., Joshi, B. C., Bagchi, M., et al. 2020b, ATel, 13799, 1
Tarter, J. 2003, ARA&A, 39, 511
Tarter, J., Cuzzi, J., Black, D., & Clark, T. 1980, Icar, 42, 136
The CHIME/FRB Collaboration, Andersen, B. C., Bandura, K. M., et al. 2020, Natur, 587, 54
Tingay, S. J., Tremblay, C., Walsh, A., & Urquhart, R. 2016, ApJL, 827, L22
Tingay, S. J., Tremblay, C. D., & Croft, S. 2018, ApJ, 856, 31
Torne, P., Eatough, R. P., Karuppusamy, R., et al. 2015, MNRAS, 451, L50
Valdes, F., & Freitas, R. A. 1986, Icar, 65, 152
Verschuur, G. L. 1973, Icar, 19, 329
von Korff, J. 2010, PhD thesis, UC Berkeley
Wharton, R. S., Chatterjee, S., Cordes, J. M., et al. 2019, ApJ, 875, 143
Worden, S. P., Drew, J., Siemion, A., et al. 2017, AcAau, 139, 98
Wordsworth, R., & Pierrehumbert, R. 2014, ApJL, 785, L20
Wright, J. T. 2018, in Handbook of Exoplanets , ed. H. J. Deeg & A. Belmonte (Berlin: Springer), 3405
Wright, J. T., Kanodia, S., & Lubar, E. 2018, AJ, 156, 260
Yao, J. M., Manchester, R. N., & Wang, N. 2017, ApJ, 835, 29
Zhang, C. F., Jiang, J. C., Men, Y. P., et al. 2020, ATel, 13699, 1